Study on 8-ary Orbital-Angular-Momentum (OAM) Shift-Keying for Free-Space Optical Communication System

MARCH 2020

Doctoral degree thesis

Tokushima University

Graduate School of Advanced Science and Technology

Munkhbayar Adiya

Abstract

The Free-space optical communication (FSO) based on 8-ary orbital angular momentum shift keying (OAM-SK), where information can be encoded as the OAM state of light, is studied. We implement a numerical simulation using a phase screen model for atmospheric turbulence, which is based on the Fourier transformation method, to analyze the influence of atmospheric turbulence. The bit error rate (BER) performance of the 8OAM-SK system is investigated in several different conditions. The numerical simulations demonstrate that higher received power is required in stronger turbulence to achieve acceptable signal quality. It is also revealed that lower data rate shows better tolerance to the turbulence strength.

Acknowledgements

First and foremost, I would like to thank my supervisors, Professor Nobuo Goto, Hiroki Kishikawa for their incite and patience in reviewing my work, answering my questions, and keeping me focused on my goals.

I thank my fellow students, who were always willing to help me overcome life and technical difficulties.

I thank my friends and family, especially my wife Nyam-Erdene Odbayar, who did countless big things that support me free to focus on my research.

I am very thankful to Tokushima University for giving me a good opportunity and supporting me all the way. I have to say that I have felt comfortable studying here. Thank you for providing a peaceful environment for the students.

Also, I would like to express my deepest appreciation to all the Japanese language teachers of the International Center at Tokushima University for their keen interest in me at every stage of my language study.

Finally, I should like to thank the members of M-JEED projects for taking the time and supporting me during my studies in Japan.

Munkhbayar Adiya

Contents

List of Figures

List of Tables

Chapter 1

Introduction

1.1 Research Background

The rapid growth of technological advances requires more bandwidth, higher speed, easy installation and responsibility on the transmission network. As a new communication technique, free-space optical (FSO) communication is one of the transmission networks that meet these requirements. The free-space optics market is estimated to reach 1223.1 million USD by 2024 with a CAGR of 36.4% between 2015 and 2024 as shown in Fig.1.1[1]. Generally it is segmented into several categories such as security, airborne application, healthcare, storage area network, data transmission, defense, disaster recovery, last mile access and others based on the applicationi types.

Orbital angular momentum (OAM) is used to enhance spectral efficiency and transmission capacity of the transmission network because of its feature. OAM provides a useful degree of freedom for increasing the information-carrying capacity of photon [2]. Laguerre Gaussian (LG) beam, widely used optical carrier of OAM, has an $\exp(im\phi)$ phase term, where m is a topological charge, and ϕ is azimuthal angle [2],[3]. Each state of OAM is orthogonal to each other, which is determined by the topological charge. Since the topological charge m is an integer and can be limitless theoretically, the transmission capacity will be improved in the FSO communication system. However, the size of the LG beam faced the limitation due to the topological charge number and all of the optical systems include finite apertures [3]-[4].

Two kinds of applications have been reported: 1) OAM- division multiplexing (OAM-DM) [5, 6] and 2) OAM - shift keying (OAM-SK) [7, 8]. 12 OAM beams, each containing 42 WDM channels on 2 polarizations, are multiplexed for achieving a communication capacity of 100Tbit/s [5]. For the OAM-SK, information is encoded into different OAM states to improve transmission quality. The FSO communication system based on OAM-SK for image transmission is implemented [8]. Moreover, some implementation of OAM-SK has been

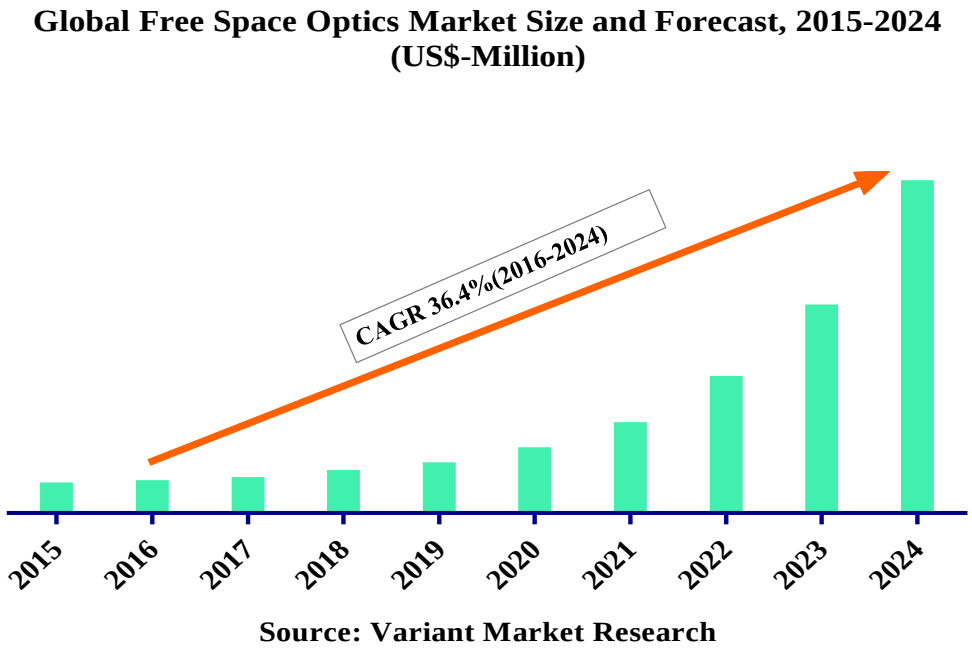

Figure 1.1: Transitions in the number of Internet users and Internet usage rates in Japan

investigated for underwater wireless optical communication [9], deep space and near-Earth optical communication [10] and convolutional neural network [11]. One of the advantages of OAM-SK compared to OAM-DM is the improving security of data transmission since the OAM modulation requires to receive a whole angular range of 2π: potential eavesdropping with a partial beam tapping would be corrupted.

FSO communication system has several challenges such as absorption, scattering, and atmospheric turbulence due to the weather and environment structure [12, 13, 14]. In particular, atmospheric turbulence plays the main role that may influence in bit error rate (BER) performance of the system. Atmospheric turbulence is a random fluctuation in the refractive index of air and it affects the intensity and phase of the transmitted signal.

In this study, the performance of the FSO communication system with the OAM-SK is studied. The effects of atmospheric turbulence on the OAM-SK are investigated through the numerical simulation. Our main goal is to find an effective method against atmospheric turbulence and noise. We implemented 2 kinds of simulations based on turbulence effects type. The first one is for the impact of phase distortion in our proposed method. In that case, we used a model named modified von Karman phase screen model for the formulation of a transmission model to investigate our new OAM-SK method in numerical simulation. Secondly, we implemented a simulation for the evaluation of the scintillation effect in our proposed method. Where we used the Gaussian distribution method for the atmospheric

turbulence channel with the scintillation effect. In both case, we operate the FSO link with turbulence over 1000 meters and used previously introduced 8 PSK label recognition circuit to implement the OAM-SK system for FSO.

1.2 Thesis Overview

The thesis is organized as follows. Section II gives the fundamentals of Free-Space Optical communication. In Section III, the modified von Karman phase screen model for turbulence and OAM beam propagation through the atmospheric turbulence are described. Our proposed OAM-SK method for the FSO communiction is illustrated on section IV. Simulation setup and analytical results are shown in Section V. Finally, Section VI presents the conclusions of our study.

Chapter 2

Fundamentals of Free Space Optical Communication

In the growing technologies era, the demand for telecommunication networks faces the necessity of more bandwidth, high speed, and easy installation. Wireless Optical Communications (WOC) is one of the greatest successes in the history of optical communication development. WOC is divided into 2 classification types depends on the transmission range: 1) Indoor and 2) Outdoor. In the indoor system, WOC links are used in a flexible interconnection between 2 or more nodes within a building where wired infrastructure is unwieldy. Outdoor/FSO links are used for long-range WOC such as terrestrial communication between two buildings/metro area extensions, and ultra-long-range WOC including ground-to-satellite/satellite-to-ground communication.

The rapidly growing use of the Internet and multimedia services requires more flexibility and responsibility. Free-space optical communication provides these requirements and it is becoming one of the key technologies for realizing very-high-speed multi-gigabit-per-second (multi-Gb/s) large-capacity aerospace communication. Also, FSO communication can be the best last-mile solution in local area networks (LANs) and metropolitan area networks (MANs) where the installation of fiber optic cables is impossible or complex. When the WorldTrade Centers collapsed on September 11th, 2001, a few wireless broadband providers used FSO technologies to solve network problems for all of the corporations within a building. It gave some opportunity to get their data networks up and running in a fraction of the time until to reinstall their wire lines[15, 16].

FSO lasercom offers several advantages over conventional RF systems, including higher data rates, narrow beam divergence, low power consumption, license-free spectrum, and security. It is used for several applications and which are introduced in the next section. Also, Free-space optical communication uses the atmospheric medium as a transmission medium so

it faces several challenges due to the impact of atmosphere and environmental characteristics.

2.1 Types of FSO communication link

Free-space optical communication is one of the best solutions of last-mile problem and space communication system where transmission speed is higher and the optical signal should be transmitted through long distance. Several applications have already introduced and implemented in practice. Generally, the FSO communication link is divided into three categories based on its application type and some examples are shown in Fig.2.1.

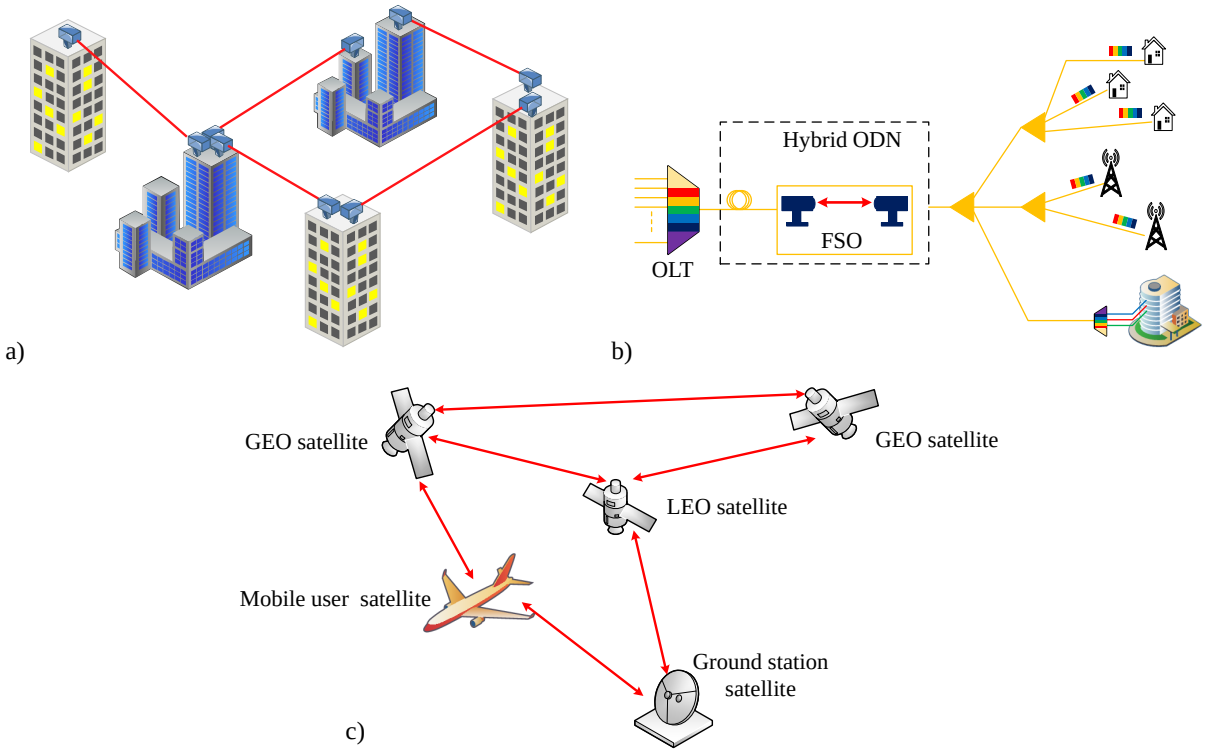

Figure 2.1: Applications of FSO communication links. a: for inter-building connections, b: for optical distribution networks (ODN), c: for aerospace communications

FSO communications link for inter-building connections: FSO communication is one of the best solutions for existing last-mile access network problems. It provides a broadband wireless access network with license-free and is used as a bridge network between one or more buildings which requires heterogeneous network traffic including high speed and freedom of license. For example, today's corporations and schools/universities are using this kind of solution for own campuses because of some advantages of FSO communication such

as easy installation, high speed, and installation cost. Also, the inter-building connection is widely used in an emergency. One of the best examples is it plays the main role of the redundant link after the 9/11 terrorist attacks in New York City.

FSO communications link for optical distribution networks (ODN): Optical Distribution Network (ODN) is the main distribution network between Optical Line Terminal (OLT) and end-users. So it should have high bandwidth and long-distance transmission. FSO reaches these requirements and it is used as an ODN for the Fiber To The Home (FTTH) applications as shown in Fig 2.1b.

FSO communications link for aerospace communications: Some examples of aerospace communications including ground-to-space, space-to-ground, and space-to-space terminal links is shown in fig 2.1c. Several projects such as Artemis (between LEO and GEO), the Japanese Optical Inter-Orbit Communications Engineering Test Satellite (between LEO-ground) had been implemented and introduced. Mobile user satellite communication is widely used by military organizations and defense companies. It collects and transfers information for aircraft-to-aircraft, aircraft-to-ground, aircraft-to-high altitude platforms (HAPs).

2.2 Structure of FSO communication

The main structure of FSO communication is almost the same with any other communication technologies and it consists of 3 basic subsystems, transmitter, transmission medium, and receiver as shown in Fig.2.2.

The first subsystem is the transmitter includes an encoder, optical source, telescope/collimator, etc. The main function of the transmitter is to modulate the information from the data source onto the optical carrier. Then, this modulated signal is propagated through the atmosphere to the receiver. Several modulation formats are usable in FSO communication. Among these modulation formats, a widely used one is intensity modulation (IM). Telescope/collimator is used to collects, collimates, and directs the optical signals to the receiver. Atmospheric transmission window is ranging 700-10000nm wavelength and 1550nm is widely used in the FSO communication system because of its advantages such as Reduced background noise and Rayleigh scattering, high transmitter power and eye-safe wavelength.

The next subsystem is transmission medium which is more complex than a traditional optical communication system. In the FSO communication system, optical signal carrying information is transmitted through the atmosphere which does not have fixed characteristics due to weather conditions and environmental structure, such as cloud, snow, fog, rain, temperature. So, it faces several challenges especially absorption, scattering, and atmospheric turbulence, etc. We will explain these atmospheric challengees in chapter 2.3.

The last subsystem is the receiver which includes receiver telescope, optical filter, pho-

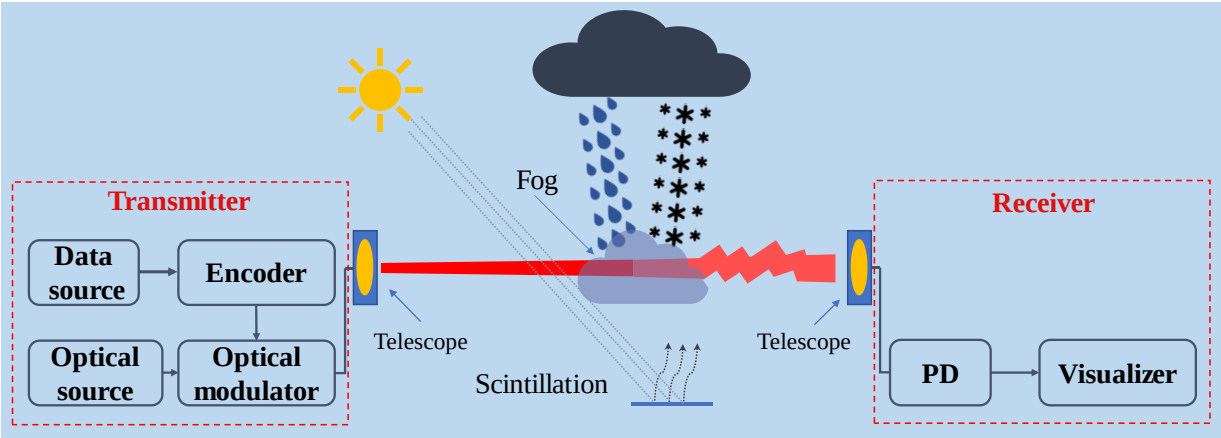

Figure 2.2: Structure of FSO communication

todetector and demodulator. The main role of the receiver is to recover the transmitted data from an optical signal. The receiver telescope collects optical radiation and directs it into a photodetector. Photodetector converts optical signal to electrical signal. An optical filter is used to reduce the level of background radiation.

2.3 Modulation and detection

Modulation can be applied to any one parameter such as intensity, phase, frequency, or the polarization of the optical carrier. Intensity modulation is implemented by varying the bias current. Frequency or phase modulation is implemented by changing the cavity length of the laser. Pulse modulation is implemented by driving current. The most commonly used modulation is intensity modulation (IM) in FSO system. IM is classified into 2 categories. 1) baseband 2) subcarrier. Generally, detection system is divided into 2 categories such as direct detection and coherent detection. Widely used detection method is direct detection system for the FSO system communication system.

2.3.1 Baseband modulation

In this kind of intensity modulation, the LED/laser drive current is directly modulated by the information signal. The information is recovered from baseband-modulated signal using direct detection technique after to be transmitted through the atmospheric channel. Baseband-modulation category includes several modulation types such as on-off keying (OOK), digital pulse-position modulation (PPM), digital pulse interval modulation (DPIM), pulse amplitude and position modulation (PAPM), and differential amplitude pulse interval modulation

(DAPIM). Among these modulation types, most popularity used modulation types are OOK and PPM because they are simple and easy to implement.

In OOK, optical ligh pulse has two modes (presence or absence) depends on the tranismission of binary. If binary is 1, led/lasertransimi is presence for the duration T_b, and if it is 0, led/laser is absence. Transmitted optical signal is attenuated due to atmospheric condition. So, OOK system requires adaptive threshold in order to prevent attenuation due to atmosphere. In other word, it is one of disadvatages of OOK in FSO communication system and OOK is more usable in short-distance FSO optical communication system.

M-PPM modulation scheme is commonly deployed for the long-distance FSO communication system. M-PPM has more power efficiency as compared to OOK because it is implemented using high peak-to average power ratio. In this kind of scheme, each symbol period is divided into M time slots (T_s), and information is placed in one of them. Here, M is equal to 2^n and n is number of symbol length. Some of example for OOK scheme and M-PPM scheme are shown in Fig.2.3. As shown in Fig.2.3, PPM scheme requires more bandwidth

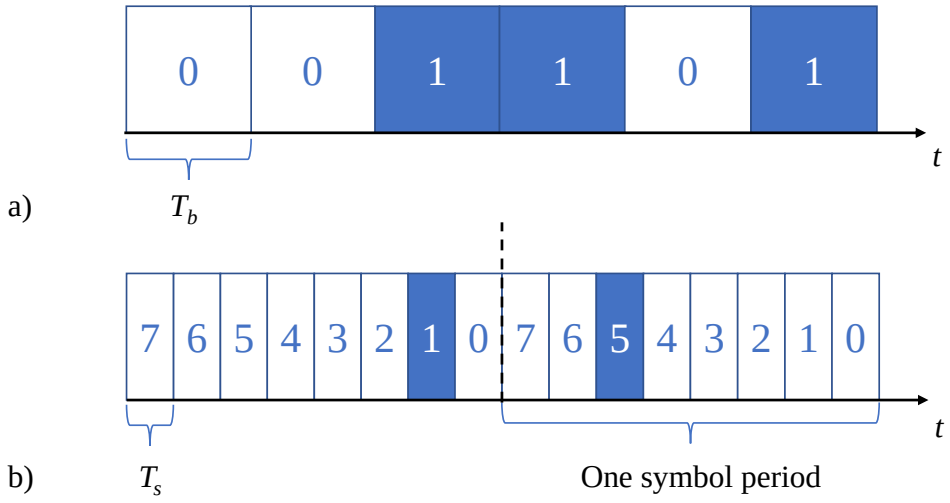

Figure 2.3: Example of modulation schemes a) OOK modulation scheme b) 8-PPM modulation scheme /transmission message = 001101/

$(= 1/T_s)$ as compared to OOK-modulated signal bandwidth $(= 1/T_b)$. Also, synchronization is complex issues in transceiver.

2.3.2 Subcarrier Modulation

A subcarrier intensity modulation (SIM) scheme uses the radio-frequency (RF) electrical signal as a subcarrier. This kind of modulation scheme is implemented with two steps. First step

is pre-modulation where RF electrical subcarrier signal is modulated with the information signal. Then, the intensity of the optical carrier is modulated using pre-modulated RF electrical carrier signal in second step. It has several advantages: does not require adaptive threshold unlike OOK, and more bandwidth efficiency. Any modulation schemes such as binary phase-shift keying (BPSK), quadrature phase-shift keying (QPSK), quadrature amplitude modulation (QAM), amplitude modulation (AM), frequency modulation (FM) can be used for the pre-modulation. Also, it provides more bandwidth efficeincy using frequency-division multiplexing (FDM). In other word, several pre-modulated electrical subcarrier signals are combined using FDM, and which is used to modulate optical carrier. Transmitted signal is recovered using direct(IM/DD)/non-coherent detection system at the receiver side.

2.3.3 Direct Detection system

Direct detection system is commonly used in FSO communication system because of its several advantages such as low cost and less complex as compare to coherent detection system. The main structure of direct detection system is shown in Fig.2.4. First element, receiver

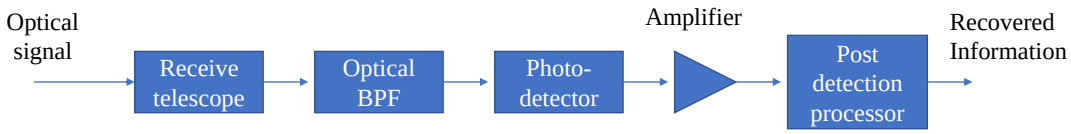

Figure 2.4: Example of modulation schemes a) OOK modulation scheme b) 8-PPM modulation scheme /transmission message = 001101/

telescope collects a optical radiation and directs it into next component. Next element is optical band-pass filter which is used to restrict the background radiation from received optical signal.Then, photodetector converts it into electrical signal and output of converted electrical signal is proportional to the instantaneous intensity of the received optical signal. Two kind of photodetectors are widely used for a partical detector (PIN and avalanche photodetector). Some noise models are used to determine the signal-to-noise ratio (SNR) of direct detection receiver. The SNR for PIN photodetector is given by

$$SNR = \frac{(R_0 P_R)^2}{2qB(R_0 P_R + R_0 P_B + I_d) + 4K_B TB/R_L}, \tag{2.1}$$

where R_0 is the detector responsivity, P_R is received power, B is the receiver bandwidth, I_d is dark current, K_B is the Boltzmann's constant, T is absolute temperature, R_L is the equivalent load resistance, and P_B the background noise power. P_R and R_0 are described by

eq.2.2 and 2.3, respectively.

$$P_R = P_T(G_T\eta_T\eta_{TP})\left(\frac{\lambda}{4\pi R}\right)^2(G_R\eta_R\eta_\lambda), \tag{2.2}$$

where P_T is transmitter power, G_T is gain of the transmitting antenna, η_T is effeciency of transmitter optics, η_{TP} is transmitter pointing loss factor, $\left(\frac{\lambda}{4\pi R}\right)^2$ is space loss factor, G_R is gain of receiving antenna, η_R is effeciency of receiver optics and η_λ is narrowband filter transmission factor.

$$R_0 = \frac{\eta q}{hf}, \tag{2.3}$$

where ν is the detector quantum efficiency, $q = 1.602 \times 10^{-19}$J is the electronic charge, $h = 6.623 \times 10^{-34}$J is the Planks's constant and f is operating frequency. The SNR for APD photodetector is given by

$$SNR = \frac{(MR_0P_R)^2}{[2qB(R_0P_R + R_0P_B + I_db)M^2F + I_{ds}] + 4K_BTB/R_L}, \tag{2.4}$$

where M is avalanche multiplication factor, F is the the excess noise factor arising due to random nature of multiplication factor, I_{db} is the bulk dark current, and I_{ds} is the surface dark current.

2.4 Challenges of FSO communication

FSO ommunication system uses atmospheric channel as a transmission link. The atmosphere channel includes several random factors such as fog, rain, haze, turbulence, etc. These factors cause random fluctuation and power loss. FSO system faces link distance limitation and random effect due to these factors. The impact level of these random factors is varying depends on the geographical location. FSO transmission link generally divided into main 2 categories depends on the transmission distance: Terrestrial links and space link. Terrestrial links are used between building-to-building, mountain-to-mountain or two ground stations. Space links are used between ground-to-satellite or satellite to satellite. To implement an FSO communication system for any cases, the system designing engineers need to have an understanding of beam propagation through atmosphere and losses.

2.4.1 Atmospheric loses

The atmosphere has a composite structure. It consists of various gases and other tiny particles. Optical signal power is reduced by these atmospheric constituents. The most popular

factors in atmospheric losses are the absorption of light by gas molecules and Rayleigh or Mie scattering. In this section, we will describe several types of losses when an optical beam is propagated through the atmospheric channel.

2.4.1.1 Absorption and scattering loss

Absorption and scattering are the main reason for the loss in the atmosphere. Which is determined by Beer's law. The received power is related to the optical depth by the determined in Beer's law [14]:

$$P_R = P_T \exp(-\tau), \tag{2.5}$$

where P_R and P_T are received and transmitted power, respectively and τ is optical depth. τ is expressed by

$$\tau = \int_0^L \gamma(p)dp, \tag{2.6}$$

The loss in dB after propogation through the atmosphere is calculated by

$$Loss = -10log_{10}T_a, \tag{2.7}$$

P_R/P_T is called that transmittance (T_a) and which is described from eq.2.5 and eq.2.6.

$$T_a = exp\left(-\int_0^L \gamma(p)dp\right), \tag{2.8}$$

where γ is total attenuation coefficient and which is sum of absorption and scattering cofficient from aerosols and molecular concentration of the atmosphere as follows [13], [14]

$$\gamma(\lambda) = \alpha_m(\lambda) + \alpha_a(\lambda), +\beta_m(\lambda) + \beta_a(\lambda), \tag{2.9}$$

The first 2 parts of eq.2.9 are molecular and aerosol absorption coefficients, respectively and last parts are molecular and aerosol scattering coefficients, respectively. The atmospheric absorption is a wavelength-dependent phenomenon [14] and some of molecular absorption coefficient are given in table.2.1 [13], [14]..

The molecular or Aerosol absorption coefficient is much smaller than the scattering coefficient and it is less than 0.2dB/km. Which is also selectively on wavelengths. Several atmospheric transmission windows within the range of 400-2400nm are used in FSO communication systems as shown in [17]. The most widely used atmospheric transmission windows for the FSO communication system are 780-850, 1520-1600 and 2000-2400nm.

The scattering process affects the angular redistribution of the optical energy with and without wavelengths. Typically, it is divided into three types depends on the radius (r) of the particles during the propagation process: Rayleigh/molecular scattering ($r < \lambda$),

Table 2.1: Molecular absorption at typical wavelengths

Wavelength (nm)	Molecular absorption (dB/km)
550	0.13
690	0.01
850	0.41
1550	0.01

Mie/Aerosol scattering ($r \approx \lambda$), and Geometric scattering ($r > \lambda$). The mass of weather conditions such as fog, haze, rain, and snow is referred to as the scattering process because these conditions have different sizes of particles as shown in table.2.2 [14], [17]. Among the scattering process, the Geometrical scattering more effectively affects the transmitted beam and the losses due to weather condition is described in the next subsection.

Another impact of atmospheric scattering is sky radiance in the day time. The scattering of solar photons on the atmospheric transmission path is the main reason for sky radiance and it creates undesirable background noise. Therefore, the signal-to-noise ratio at the receiver is degraded by the background noise. Received background noise depends on several factors such as the geometry of the receiver and relative location of the sun and transmitter.

2.4.1.2 Loss due to weather condition

The data is transmitted through the atmospheric channel in the FSO communication system. So, the performance of the FSO communication system depends on the environmental factors including weather conditions such as fog, snow, and rain. The optical signal is distorted due to those weather conditions because it has absorption, scattering, and reflection. The main

Table 2.2: The typical atmospheric particles and type of scattering process .

Type of particles	Radius (r)	Type of scattering process
Air moleculus	0.0001	Rayleigh
Haze particle	0.01-1	Rayleigh-Mie
Fog droplet	1-20	Mie-Geometrical
Rain	100-10,000	Geometrical
Snow	1000-5000	Geometrical
Hail	5000-50,000	Geometrical

measure is visibility to determine the strength of loss due to weather conditions. It is a distance that transmitted optical signal intensity reaches 2% of original value through the parallel luminous beam travels a path in the atmosphere. The specific attenuation due to fog, snow, and rain is described below.

Fog/Haze: The attenuation due to fog/haze has Mie/rayleigh scattering process as shown in table.2.2. It is calculated by the visibility range information-based method. Which is described in eq.2.10.

$$\beta_{fog}(\lambda) = \frac{3.91}{V}\left(\frac{\lambda}{550}\right)^{-p}, \tag{2.10}$$

where the wavelength of 550nm is reference wavelength for common empirical models, p is the size distribution coefficient of scattering, λ is operation wavelength (nm), and V is visibility range (km). The size distribution coefficient of scattering is based on the visibility range and gets different values for the empirical models. Widely used models are Kim and Kruse model, p is given as an eq.2.11 and 2.12, respectively.

$$p = \begin{cases} 1.6 & V > 50 \\ 1.3 & 6 < V < 50 \\ 0.16V + 0.34 & 1 < V < 6 \\ V - 0.5 & 0.5 < V < 1 \\ 0 & V < 0.5 \end{cases} \tag{2.11}$$

$$p = \begin{cases} 1.6 & V > 50 \\ 1.3 & 6 < V < 50 \\ 0.585V^{1/3} & V < 6 \end{cases} \tag{2.12}$$

The relation between visibility range and attenuation for some of the weather conditions at 1550nm is shown in table.2.3.

Fig.2.5a and Fig.2.5b show an attenuation vs visibility graph at the low visibility range weather condition (0.2-6km), for Kim's model and Kruse model, respectively. Operation wavelength of 1550nm has quiet less attenuation than compared to the others as shown in both graphs. The same characteristic observed at the high visibility weather condition ($6km < V$) as shown in Fig.2.5c. Both of model has the same size distribution coefficient of scattering for V>6km weather condition.

Rain: Rain creates a non-selective scattering process and attenuation due to rain depends on the rain rate. The specific attenuation (dB/km) is expressed for rain rate (mm/hr) in eq.2.13.

$$\beta_{rain} = m_1 R^{m_2}, \tag{2.13}$$

where R is rain rate in mm/hr, m_1 and m_2 are the model parameters. Table.2.4 [13], [14] gives values of those parameters as recommended by International Telecommunication Union

Table 2.3: The relation between weather condition and visibility range

Weather condition	Visibility range (km)	Loss (dB/km) at 1550nm (Kim's model)	Loss (dB/km) at 1550nm (Kruse model)
1 Thick fog	0.2	19.55	13.71
Moderate fog	0.5	7.82	4.83
Light Fog	0.77-1	3.83-3.91	2.91-2.13
Thin fog/heavy rain (25mm/hr)	1.9-2	1.05-0.98	0.97-0.91
Haze/medium rain (12.5mm/hr)	2.8-4	0.61-0.35	0.59-0.37
Light haze/light rain (2.5mm/hr)	5.9-10	0.17-0.1	0.22-0.1
Clear/drizzle)(0.25mm/hr)	18-20	0.056-0.05	0.056-0.05
Very clear	23-50	0.044-0.014	0.044-0.014

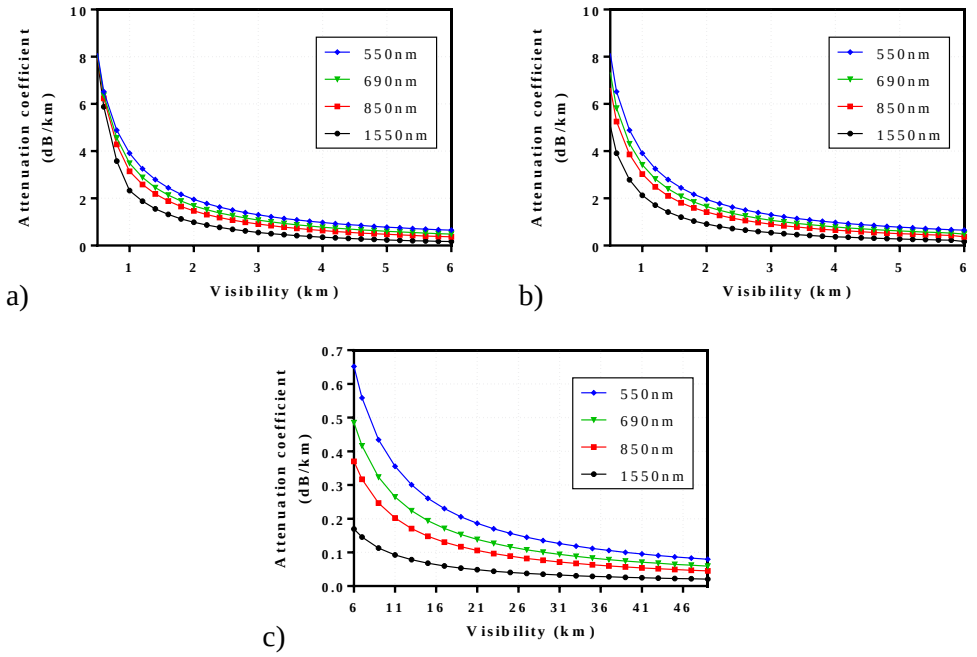

Figure 2.5: Attenuation vs visibility

- Radiocommunication (ITU-R).

Table 2.4: Molecular absorption at typical wavelengths.

Model	Origin	m_1	m_2
Carbonneau	France	1.076	0.67
Japan	Japan	1.58	0.63

The rain attenuation based on visibility range can be expressed by

$$\alpha_{rain} = \frac{2.8}{V}, \tag{2.14}$$

Snow: Attenuation due to snow depends upon snowflake and snow rate. The specific attenuation (dB/km) is categorized into 2 types for snow and is expressed for snow rate (mm/hr) in eq.2.15.

$$\beta_{snow} = aS^b, \tag{2.15}$$

where S is snow rate, the values of parameters a and b in dry and wet snow are

$$\begin{aligned} \textbf{Dry snow:}&\text{a}=5.42\times10^{-5}+5.4958776, \qquad b=1.38 \\ \textbf{Wet snow:}&\text{a}=1.023\times10^{-4}+3.7855466, \qquad b=0.72 \end{aligned} \tag{2.16}$$

The snow attenuation based on visibility range can be expressed by

$$\alpha_{snow} = \frac{58}{V}, \tag{2.17}$$

2.4.1.3 Free-Space loss

Space loss is one of the biggest losses in the FSO system because the signal is propagated through the free-space. The space loss is expressed by

$$L_s = \left(\frac{\lambda}{4\pi R}\right)^2, \tag{2.18}$$

where λ is operation wavelength and R is propagation distance. The FSO communication system has smaller space loss compare with RF communication systems due to dependence on the wavelength as shown in eq.2.18. Naturally, this loss is higher at long distance and the FSO communication system faces limitations in link range due to space loss.

2.4.1.4 Geometrical loss

In the FSO communication system, the optical beam spreads out due to diffraction while it propagates through the atmosphere. It is a reason of geometrical path loss/beam divergence

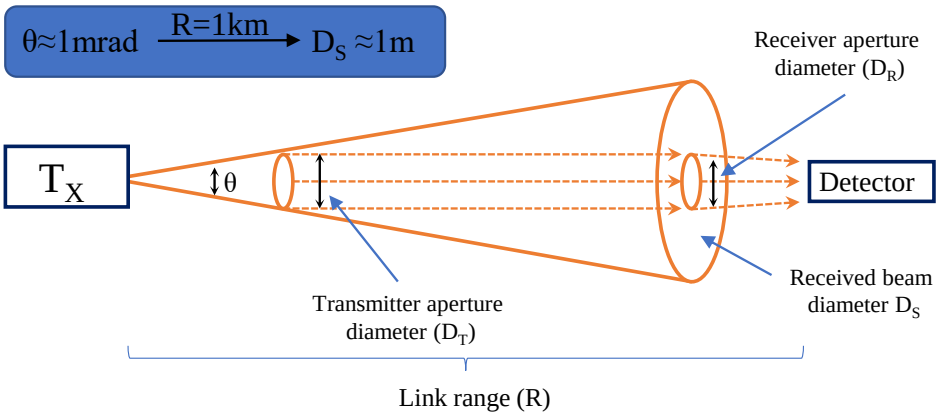

Figure 2.6: Structure of FSO communication

loss. Transmitter and receiver aperture diameters are quantifiable parameters because which's sizes are usually specified by the manufacturer and the receiver aperture size should be more sizeable to collect a fraction of the transmitted beam without any losses. But, little value of beam divergence angle makes more large received beam diameter (D_S) as shown in fig.2.6. Table.2.5 [17] illustrates the relation between divergence (mrad) and received beam diameter (m) at 1km ling range.

Table 2.5: The divergence and received beam diameter .

Divergence	Received beam diameter (D_S)
0.5mrad	$\approx$ 0.5m
1mrad	$\approx$ 1m
2mrad	$\approx$ 2m
4mrad	$\approx$ 4m

For non-diffraction-limited case, transmitance is expressed by [14]

$$\frac{P_R}{P_T} = \frac{D_R^2}{(D_T + \theta_{div} + R)^2} \tag{2.19}$$

and geomethrical path/divergence loss in dB will be [14]

$$L_{Geometrical} = -20log\left[\frac{D_R}{(D_T + \theta_{div} + R)}\right] \tag{2.20}$$

2.4.2 Atmospheric turbulence

Atmospheric turbulence is a random phenomenon due to the change in temperature, pressure, and wind variation. It affects the propagation of an optical beam and causes a phase shifts of the optical beam. It is a major reason for wavefront distortion after transmitted through the atmosphere. The changes in temperature, pressure, and wind variation produce refractive index variations in the air. And, these variations are referred to as eddies which are unstable air masses. These eddies are divided into 2 scales depend on their size. The outer scale L_0 is in the order of about 10-100m and the inner scale l_0 is in the order of about 1-10mm. These eddies lead to distortion in the phase and intensity of the received signal because it has qualification with random fluctuations. In other words, these eddies work like lens or prism. Atmospheric turbulence leads to several effects such as beam wandering, beam spreading, and beam scintillation on optical beam.

2.4.2.1 The refractive index structure

The refractive index structure parameter C_n^2 determines the strength of turbulence. It depends on the altitude, location, and time of day. The coast, also known as the coastline or seashore, has a larger refractive index structure because where the air density is higher. C_n^2 is almost constant for the near ground horizontal link. Its typical value is 10^{-17} $\mathrm{m}^{-3/2}$ for the weak turbulence and 10^{-13} $\mathrm{m}^{-}3/2$ or larger for strong turbulence. Several models for C_n^2 are commmonly used and which are listed on the table.2.6 [13]. Among those models, one of the more used is Hufnagel-Valley model and which is given by [17]

$$\begin{aligned} C_n^2 &= 0.00594\left(\frac{\nu}{27}\right)^2 (10^{-5}h)^{10}\exp\left(\frac{h}{1000}\right) \\ &+2.7\times 10^{-16}\exp\left(\frac{h}{1500}\right) + A_0\exp\left(\frac{h}{100}\right) \end{aligned} \tag{2.21}$$

where h is the altitude in [m], ν is the wind speed at high altitude [m/s], A_0 is the turbulence strength at the ground level, $A_0 = 1.7\times 10^{-14}m^{-2/3}$

2.4.2.2 Beam wandering due to turbulence

When the eddies size of turbulence is larger than the optical beam size, the beam bends from its transmission path. This phenomenon is named that beam wandering and it leads to pointing error displacement of the beam. Beam wandering displacement is given by

$$\sigma_{BW}^2 = 1.44C_n^2L^2W_0^{-1/3} \tag{2.22}$$

where L is link length and W_0 is initial beam size.

Table 2.6: Turbuence profile models for C_n^2.

	Models	Range	Comments
1	PAMELA	Long (few tens of kms)	- Robust model for different terrains and weather type - Sensitive to wind speed - Does not perform well over marine/overseas environment
2	NSLOT	Long (few tens of kms)	- More accurate model for marine propagation - Surface roughness is 'hard-wired' in this model - Temperature inversion
3	Fried	Short in meters	- Support weak, strong and moderate turbulence
4	Hufnagel & Stanley	Long (few tens of kms)	- C_n^2 is proportional to h^{-1} - Not suitable for various site conditions
5	Hufnagel Valley	Long (few tens of kms)	- Most popular model as it allows easy variation of day and night time profile by varying various site parameters lik wind speed, iso-planatic angle and altitude - Best suited for ground to satellite uplink
6	Gurvich	Long (few tens of kms)	- Covers all regimes of turbulence from weak, moderate to strong
7	Von Karman - Tatarskii	Medium (few kms)	- Make use of phase peturbations of laser beam to estimate inner and outer scale of turbulence - Sensitive to change in temperature difference
8	Greenwood	Long (few tens of kms)	- Night time turbulence model for astronomical imaging from mountaintop site
9	Submarine Laser - communication	Long (few tens of kms)	- Well suited for day time turbulence profile at island site - Developed for AMOS observatory in Maui, Hawai
10	Clear 1 -	Long (few tens of kms)	- Well suited for night time turbulent profile - Averages and statistically interpolate radiosonde observation measurements obtained from large number of meteorological condistions

2.4.2.3 Beam spreading due to turbulence

When the eddies' size of turbulence is smaller than the optical beam size, the optical beam is diffracted and scattered. It causes the received wavefront. This phenomenon is named that beam spreading and one way to prevent method beam spreading is to increase the receiver aperture average-size. In other words, the bigger aperture size is suitable to use in the FSO system.

2.4.2.4 Scintillation due to turbulence

When the eddies size of turbulence is around beam size, the phenomena named scintillation is observed in the atmospheric medium. Which acts like a lens that will focus and de-focus the incoming beam [13]. It causes loss of signal-to-noise ratio and sets a fluctuation in intensity of the incoming beam. Scintillation is one of the major causes of a reduction in the performance of FSO communication system. The σ_i^2 is the scintillation index parameter which determines the strength of the turbulence and describes an intensity fluctuation with the normalized variance. It is given by

$$\sigma_i^2 == \frac{\langle I^2 \rangle - \langle I \rangle^2}{\langle I \rangle^2} = \frac{\langle I^2 \rangle}{\langle I \rangle^2} - 1, \tag{2.23}$$

where I is the signal irradiance or intensity.

In weak turbulence, $\sigma_i^2 < 1$, the intensity statistic is given by log-normal distribution and scintillation index is expressed as

$$\sigma_i^2 = \sigma_R^2 = 1.23 C_n^2 k^{7/6} R^{11/6} \qquad \textbf{for plane wave}, \tag{2.24}$$

$$\sigma_i^2 = 0.4\sigma_R^2 = 0.5 C_n^2 k^{7/6} R^{11/6} \qquad \textbf{for spherical wave}, \tag{2.25}$$

where k is wavenumber $(2\pi/\lambda)$, σ_R^2 is the Rytov variance, and R is link range. In strong turbulence, $\sigma_i^2 \geq 1$, the intensity statistic is Rayleigh distributed and scintillation index is expressed as

$$\sigma_i^2 = 1 + \frac{0.86}{\sigma_R^{4/5}} \quad \sigma_R^2 >> 1 \qquad \textbf{for plane wave}, \tag{2.26}$$

$$\sigma_i^2 = 1 + \frac{2.73}{\sigma_R^{4/5}} \quad \sigma_R^2 >> 1 \qquad \textbf{for spherical wave}, \tag{2.27}$$

There are various mathematical models are used for probability density function (PDF) in the FSO communication channel model. In general, these mathematical models are divided into 3 categories depends on the strength of turbulence. The first category is a channel model with weak turbulence. In this model, the irradiance statistic is given by log-normal

models. Second and third categories are moderate and strong turbulence channel models, respectively.

Log-Normal distribution: This distribution is valid for weak turbulence with short distance (100m) and the PDF of Log-Normal distribution is given by

$$f(I) = \frac{1}{\sqrt{2\pi\sigma_i^2}} \frac{1}{I} \exp\left(-\frac{(\ln(I/I_0) + \sigma_i^2/2)^2}{2\sigma_i^2}\right) \tag{2.28}$$

where I_0 is the irradiance in the absence of turbulence.

I-G distribution: Inverse-Gaussian distribution is modeled as an alternative of Log-Normal distribution. It is also used for weak turbulence modeling and the PDF of I-G distribution is given by

$$f(I) = \sqrt{\frac{\lambda}{2\pi I^3}} \exp\left(-\frac{\lambda(1-\mu)^2}{2\mu^2}\right), \qquad I > 0 \tag{2.29}$$

where $\mu > 0$ is the mean of fluctuation parameter and $\lambda > 0$ is a distribution scale parameter.

Negative exponential distribution: It is used for strong turbulence modeling with long-distance (several kms) and the PDF of NE distribution is given by

$$f(I) = \frac{1}{I_0} \exp\left(-\frac{-I}{I_0}\right), \qquad I_0 > 0 \tag{2.30}$$

where I_0 is the mean irradiance.

Gamma-Gamma distribution: It is modeled for moderate to strong turbulence modeling with long-distance (several kms). Which includes two random variables (small scale - α, large scale-β eddies) and the PDF of GG distribution is given by

$$f(I) = \frac{2(\alpha\beta)^{(\alpha+\beta)/2}}{\Gamma(\alpha)\Gamma(\beta)} I^{(\alpha+\beta)/2-1} K_{\alpha-\beta}(2\sqrt{\alpha\beta I}), \qquad I > 0 \tag{2.31}$$

where $K_a(.)$ is the modified Bessel function of order a. α and β are the effective number of the small and large scale of eddies, respectively and given by

$$\alpha = \left[\exp\left(\frac{0.49\sigma_i^2}{\left(1 + 1.11\sigma_i^{12/5}\right)^{7/6}}\right) - 1\right]^{-1} \tag{2.32}$$

$$\beta = \left[\exp\left(\frac{0.51\sigma_i^2}{\left(1 + 0.69\sigma_i^{12/5}\right)^{7/6}}\right) - 1\right]^{-1} \tag{2.33}$$

K-distribution: It is modeled for strong turbulence modeling. It is a combination of exponential distribution and gamma distribution. The PDF of K-distribution is given by

$$f(I_{mn}) = \frac{2\alpha_{mn}^{(\alpha_{mn}+1)/2}}{\Gamma(\alpha_{mn})} I_{mn}^{(\alpha_{mn}-1)/2} K_{\alpha_{mn}-1}(2\sqrt{\alpha_{mn} I_{mn}}), \qquad I_{mn} > 0 \tag{2.34}$$

where $K_v(.)$ is the modified Bessel function of second kind of order v, α_{mn} is the parameter related to the discrete number of scatters, and $\Gamma(.)$ is the Gamma function.

I-K distribution: It is modeled for weak to strong turbulence modeling. The PDF of I-K distribution is given by

$$f(I) = \begin{cases} 2\alpha(1+\rho)\,(1+1/\rho)^{(\alpha-1)/2}\, K_{\alpha-1}(2\sqrt{\alpha\rho}) I_{\alpha-1}(2\sqrt{\alpha(1+\rho)I}), & 0 < I < \dfrac{\rho}{1+\rho} \\ 2\alpha(1+\rho)\,(1+1/\rho)^{(\alpha-1)/2}\, I_{\alpha-1}(2\sqrt{\alpha\rho}) K_{\alpha-1}(2\sqrt{\alpha(1+\rho)I}), & I > \dfrac{\rho}{1+\rho} \end{cases} \tag{2.35}$$

where $I_a(.)$ is the modified Bessel function of first kind of order a, ρ is a measure of the power ratio of mean intensities of coherent.

Chapter 3

The OAM beam propagation through atmospheric turbulence

When light propagates through the free-space, it is possible to change its intensity profile during propagation. In other words, optical beam with different electric field amplitude distribution, which is called modes, can be created in free-space optical communication using re-scaling of the profile, change in optical phase, and change in the total optical power. Optical beams such as Laguerre-Gaussian (LG), Bessel-Gaussian (BG) and Hermite-Gaussian can carry OAM. In this chapter, we will illustrate some of the OAM beams and phase screen models for atmospheric turbulence.

3.1 Hermite-Gaussian beam

The electric field distributions of Hermite-Gaussian beams are determined by the combination of a Gaussian function and a Hermite polynomial which is described as:

$$\begin{aligned} u_{HG}(r,\phi) = H_p\left(\frac{\sqrt{2}x}{w_{0x}}\right)\exp\left(-\frac{x^2}{w_{0x}^2}\right)\exp\left(j\frac{\pi x^2}{\lambda R_{0x}}\right) \\ \times H_m\left(\frac{\sqrt{2}y}{w_0 y}\right)\exp\left(-\frac{y^2}{w_{0y}^2}\right)\exp\left(j\frac{\pi y^2}{\lambda R_{0y}}\right) \end{aligned} \tag{3.1}$$

where p and m represent the X and Y index that decribe the mode dependencies for X and Y-axis. R is the radius of curvature and w_0 is the spot size. H_p and H_m are the Hermite polynomials.

Fig.3.1 shows the some example for intensity profiles of Hermite-Gaussian beams. Which has $p+1$ nodes in the horizontal direction and $m+1$ nodes in the vertical direction. A

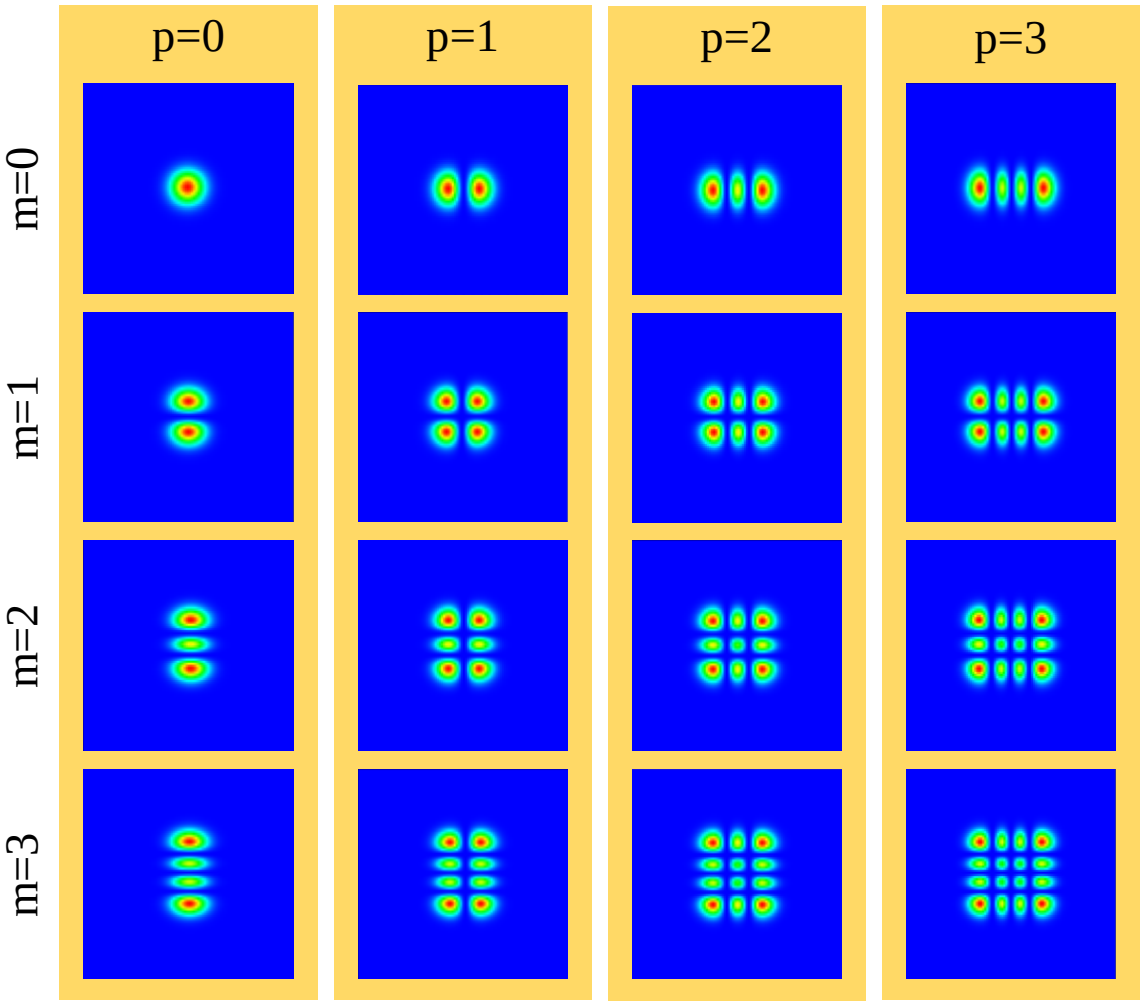

Figure 3.1: Intensity profiles of HG beams

Gaussian beam, which is named that fundamental mode or axial mode, has highest beam quality and where $p = m = 0$ as shown in upper left-hand side of Fig.3.1.

3.2 Bessel-Gaussian beam

In practical condition, ideal Bessel beam is not possible and Bessel-Gaussian beam is more experimentally formed with complex field amplitude. Which is one of the special OAM beams based on the Bessel's function and expressed as [3],[18]

$$u_{BG}(\rho, \phi) = J_m(k_r \rho) \exp(im\phi) \exp\left(-\frac{\rho^2}{w_g^2}\right), \tag{3.2}$$

where w_g is beam waist and J_m is the first kind of m-th order Bessel function.

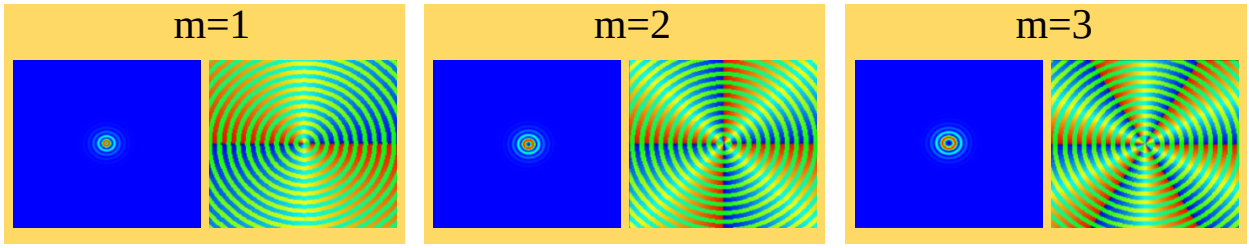

Figure 3.2: Intensity and phase profiles of BG beams

Fig.3.2 shows some examples of the Intensity and Phase profile of Bessel-Gaussian beams.

3.3 Laguerre-Gaussian beam

The LG beams are widely used in OAM-DM and OAM-SK systems [19, 20]. In the cylindrical coordinates the optical field distribution of LG_{pm} beam can be expressed as [9, 10],[19],[20]

$$u_{LG}(r,\phi,z) = R_{pm}(r,z)\exp(-im\phi), \tag{3.3}$$

where m is the angular index of the OAM mode (known as a topological charge) and $R_{pm}(r,z)$ is the radial basis function expressed as follows:

$$\begin{aligned} R_{pm}(r,z) = \sqrt{\frac{2p!}{\pi(p+|m|)!}}\frac{1}{w(z)}\left[\frac{\sqrt{2}r}{w(z)}\right]^{|m|} \times L_p^{|m|}\left[\frac{2r^2}{w^2(z)}\right] \\ \times \exp\left[-\left(\frac{r^2}{w^2(z)}\right)\right] \times \exp\left[\frac{-ikr^2z}{2(z^2+z_R^2)}\right] \\ \times \exp\left[i(2p+|m|+1)\tan^{-1}\frac{z}{z_R}\right] \end{aligned} \tag{3.4}$$

where $w(z)$=$w_0\sqrt{1+(z/z_R)^2}$ is the beam radius at distance z, in which w_0 is the zero-order Gaussian radius at the waist, z_R=$\pi w_0^2/\lambda$ is the Rayleigh range, λ is optical wavelength, and k=$2\pi/\lambda$ is the wave number.

Fig 3.1 shows the intensity and phase profile of LG beams. The term $L_p^m(\ )$ represents the generalized Laguerre polynomial in eq 3.2, and p is a radial mode number. When $p=0$, $L_p^m(\ )$ will be unity. In that case, the intensity of LG beam forms is a ring, whose radius is proportional to $\sqrt{m}$ as shown in Fig 3.1. An angular index m of the OAM mode mainly affects the radius and thickness. In another case ($p \neq 0$), the intensity of LG beam form will become several rings and outside ring size becomes mores bigger depends on radial mode number as shown in second and third row in Fig 3.1. Fig 3.2 shows the phase profiles of Laguerre-Gaussian beams.

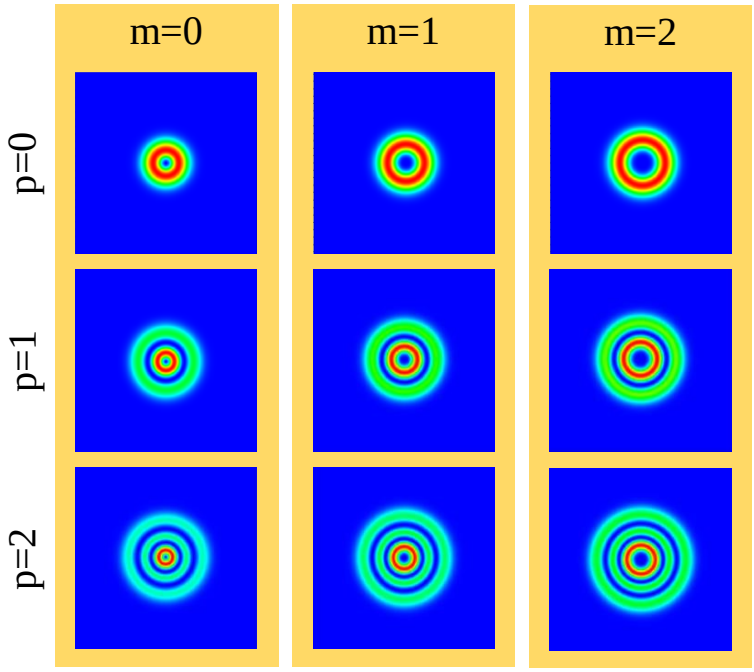

Figure 3.3: Intensity profiles of LG beams

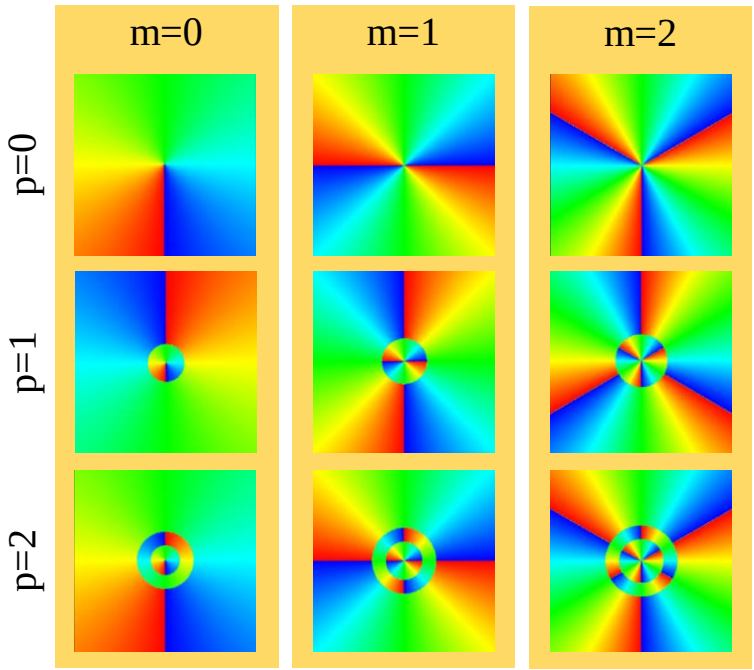

Figure 3.4: Phase profiles of LG beams

3.4 Turbulence phase screen model

In FSO communication, researchers have been paid attention to the effects of turbulence. They have been used several models to evaluate the effects of turbulence. Turbulence has major two impacts of scintillation and phase distortion. Two kinds of phase screen models are used for the study of phase distortion such as Kolmogorov phase screen [21] and non-Kolmogorov phase screen [22]. Between these phase screen models, Kolmogorov' s phase screen is expressed by the most widely accepted theory of turbulent flow. There are commonly used models based on Kolmogorov such as the Tatarskii [23, 24], von Karman [24, 25], modified von Karman [24], and Hill spectrum [26, 27]. We use the modified von Karman (mvK) phase screen model in this research. The power spectrum density (PSD) function of the phase fluctuation due to turbulent air is expressed as[24, 28]

$$\Phi_{\phi}^{mvK}(f) = 0.023 r_0^{-5/3} \frac{\exp -f^2/f_m^2}{(f^2 + f_0^2)^{11/6}}, \tag{3.5}$$

where f is the spatial frequency, $f_m = 5.92/l_0/2\pi$ is the inner scale frequency, $f_0 = 1/L_0$ is the outer scale frequency, l_0 and L_0 are the inner and outer scales of turbulence, and r_0 is Fried parameter described by

$$r_0 = \left[0.423 k^2 C_n^2 \Delta z\right]^{-3/5}, \tag{3.6}$$

where C_n^2 is the refractive index structure parameter representing turbulence strength and Δz is the distance of propagation. The fast Fourier transform (FFT) based method [21, 29, 30] is used to generate a complex Gaussian random matrix using the mvK power spectrum of the atmospheric turbulence. Note that the real and imaginary parts of the inverse FT (IFT) produce two uncorrelated phase screens. In our research, we used a real part of the IFT product and this process is expressed by

$$PS = real\big(IFT(\Phi_{\phi}^{mvK}) \times r(x, y)\big), \tag{3.7}$$

where $r(x, y)$ is the complex Gaussian distribution of random variables with zero mean and unit variance.

Some example of mvK phase screen of turbulence with different turbulence strength at 1 km propagation distance is shown in Fig.3.5. More strength turbulence makes more strong phase distortion on the transmitted beam as shown in this figure.

Also, a phase screen on different propagation distances with weak turbulence is shown in Fig.3.6. The maximum phase distortion is 0.81, 1, and 1.8 rad for the 100m, 500m, and 700m, respectively.

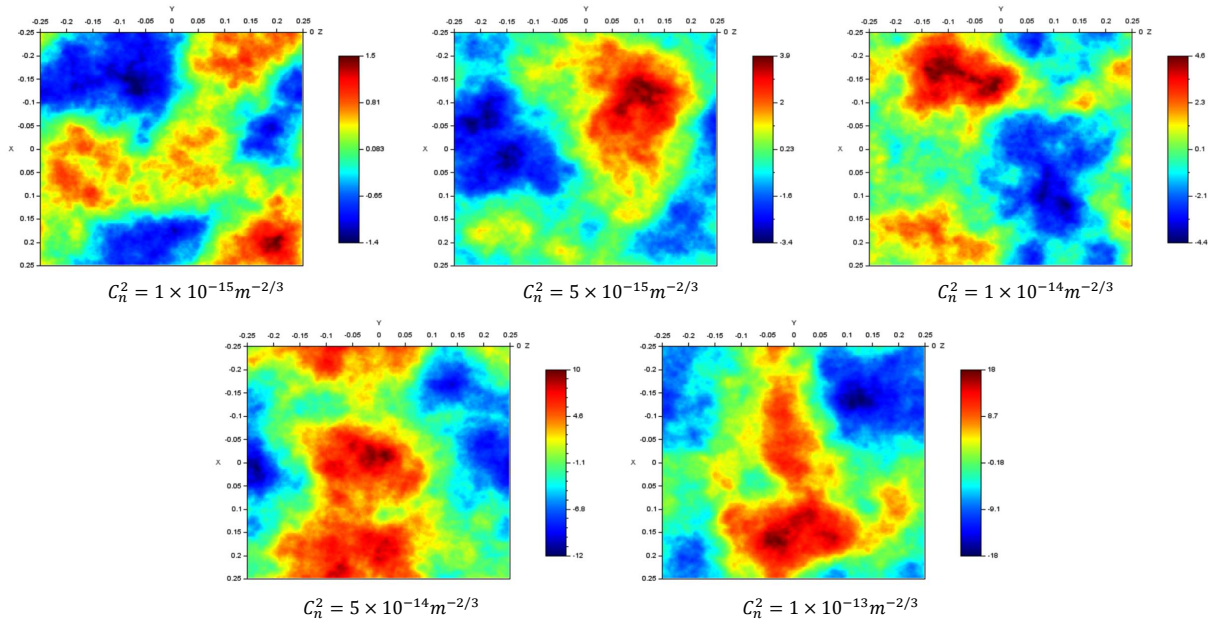

Figure 3.5: mvK phase screen with different turbulence strengths at 1km

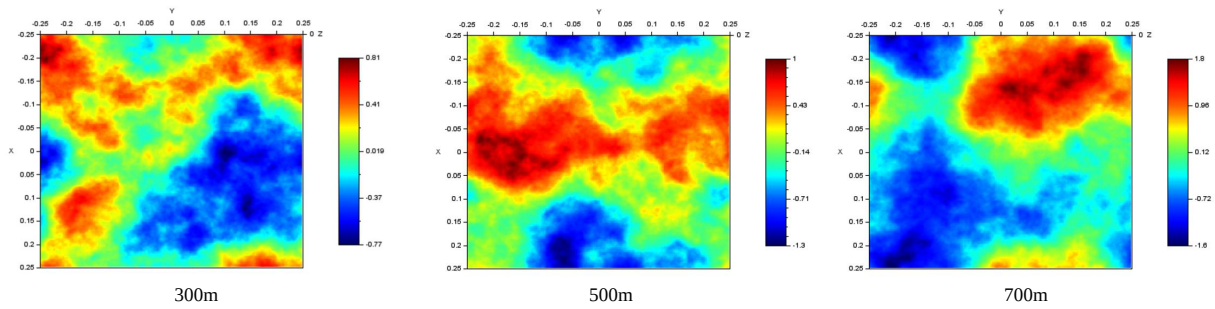

Figure 3.6: mvK phase screen with different distances at $C_n^2 = 5 \times 10^{-14} m^{-2/3}$

3.5 Laguarre-Gaussian beam propagation through the atmospheric turbulence

One and two-step propagation methods with a Fresnel-diffraction theory for propagation calculation are widely used in optical communication system simulation. The one-step method has some disadvantages such as a trade-off problem between source and observation grids. The two-step propagation method gives an opportunity to select the flexibility grids which is presented by Coy and Rydberg and Bengtsson [28]. So, we use the two-step propagation

method.

Optical field distribution of LG beam after turbulence could be expressed by

$$u_{LG}^{'}(r,\phi,z) = u_{LG} \times \exp(iPS) \tag{3.8}$$

Some examples of mvK phase screen model and influence on the transmitted LG beam are shown in Fig.3.7. The phase distribution of the transmitted beam is distorted by atmospheric turbulence depending on the turbulence strength. Laguerre-Gaussian beams are orthogonal

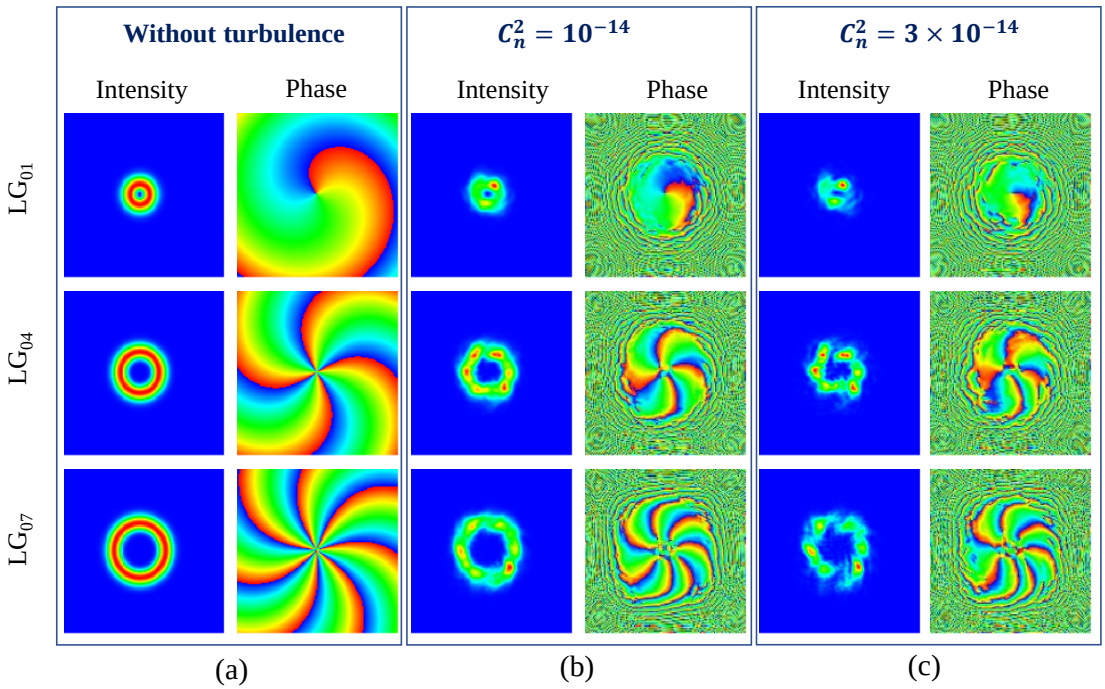

Figure 3.7: Intensity and phase distributions under different strength of atmospheric turbulence as (a) without turbulence, (b) moderate turbulence $C_n^2 = 1 \times 10^{-14} m^{-2/3}$, and (c) strong turbulence $C_n^2 = 3 \times 10^{-14} m^{-2/3}$ for LG beams with $m = 1, 4$, and 7, $w_0 = 4$cm, and propagation length $z = 500$m.

to each other and it can be expressed by the combination of LG modes. Therefore, received OAM beam can be expressed by decomposition of each deformed received OAM modes after the impact of atmospheric turbulence. In other words, a received OAM beam is a set of transmitted beam mode and its neighbor modes. The power of these neighbor modes is not fixed due to the strength of atmospheric turbulence. So, the power difference between original OAM mode and neighbor is variable which is named crosstalk. A strongly distorted beam has strongly crosstalk with neighbors.The leakage of each demodulated received OAM mode to its neighboring for the 4 different cases is shown in Fig.3.8. First case is without

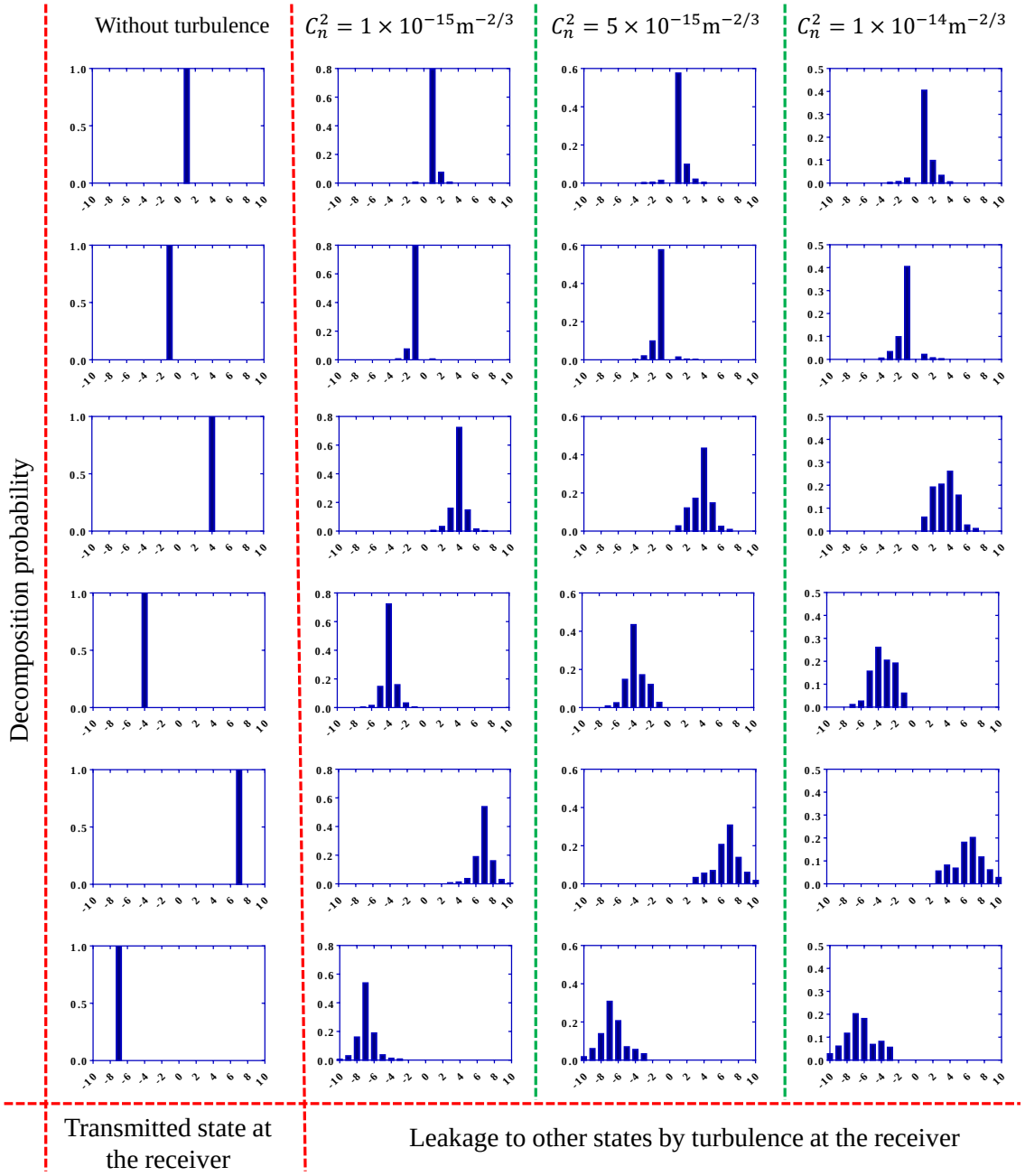

Figure 3.8: The leakage of each demodulated received OAM mode to its neighboring. (without turbulence, $C_n^2 = 1 \times 10^{-15} m^{-2/3}$, $C_n^2 = 5 \times 10^{-15} m^{-2/3}$ and $C_n^2 = 1 \times 10^{-14} m^{-2/3}$ for LG beams with $m = 1, -4, and + 7$, $w_0 = 4$c; and propagation length $z = 1000$m.

any turbulence. In that case, transmitted OAM state is fully deformed at the receiver. In other cases, turbulence strength is $C_n^2 = 1 \times 10^{-15} m^{-2/3}$, $C_n^2 = 5 \times 10^{-15} m^{-2/3}$ and

$C_n^2 = 1 \times 10^{-14} m^{-2/3}$ with 1000m propagation distance. As shown in graph, leakage is higher as the strength of turbulence icreases. For example, for transmitted OAM state is +1, the decomposition probability is 0.8, 0.58, and 0.4 when turulence strength $C_n^2 = 1 \times 10^{-15}, 5 \times 10^{-15}$,and $1 \times 10^{-14}, m^{-2/3}$, respetively. Simultaneously, same result is investigated on the other OAM statas is decreased by the turbulence strength. Also power difference between transmitted OAM mode and neighbor modes Moreover, bigger the topological charge has a stronger the leakage. For example, when turulence strength $C_n^2 = 1 \times 10^{-14}$, decomposition probability is 0.2 for $l = +7$. It is two times smaller than case with $l = +1$. So, more step away mode selection method is usable in OAM-DM or OAM-SK sysem to prevent from power leakage and decrease the relation between used OAM modes.

Chapter 4

Concept of OAM-SK

In this section, we describe the OAM-SK-FSO transmission system. The schematic diagram is shown in Fig.4.1. It consists of 3 major parts including transmitter, transmission medium, and receiver. In the transmitter side, an LG beam with a single TC is selectively generated by using an encoder and spatial light modulators (SLMs) in a one-symbol period depending on the bit-sequence. A three-bit sequence is converted to an individual OAM mode in this system. We use eight OAM beams assumed to have TCs of $m_1 = -10$, $m_2 = -7$, $m_3 = -4$, $m_4 = -1$, $m_5 = +1$, $m_6 = +4$, $m_7 = +7$, and $m_8 = +10$. This mode selection is based on the literature [19], in which the optimal mode sets have been discussed by considering the mode crosstalk after free-space propagation of OAM-DM beams in the atmospheric turbulent link. It is worth noting that the OAM-SK, which transmits a single mode in a one-symbol period, has the different influence of the turbulence from OAM-DM. Although the transmitted single OAM mode is decomposed into several modes like a Gaussian distribution due to the distortion caused by the atmospheric turbulence, it does not have crosstalk from other modes while in the turbulent link propagation since there is a single-mode in a one-symbol period when inter-symbol interference is negligible. In the receiver side, the bit sequence is retrieved

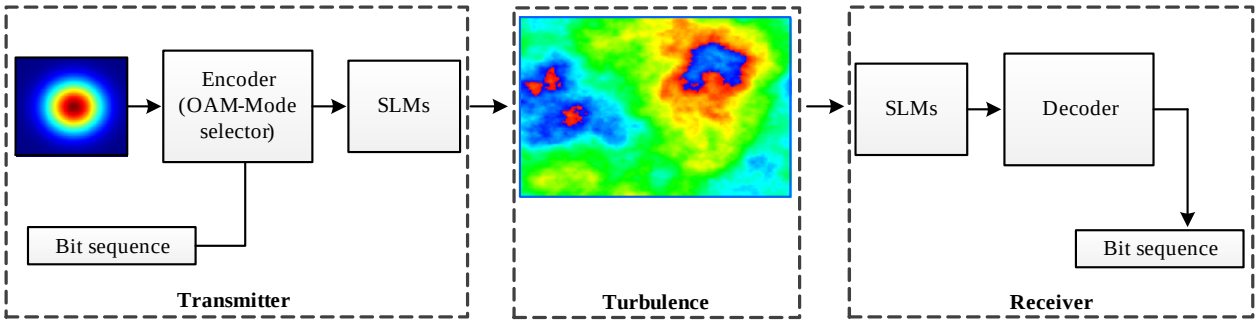

Figure 4.1: The schematic diagram of OAM-SK for FSO system

by comparing and finding a mode having the highest power between the selected modes from m_1 to m_8. At this receiving procedure, the approach of the optimal mode sets selection succeeds since the mode spacing over 1 effectively avoids detecting the neighboring mode having relatively high power. We choose four modes from $m_5 = +1$ to $m_8 = +10$ with the mode spacing of 3 and four their negative modes from $m_4 = -1$ to $m_1 = -10$ to mitigate the influence of mode decomposition and to enhance the received signal quality as possible. Then, an optical signal with 8-ary OAM-SK is transmitted through the FSO channel with atmospheric turbulence which is explained in chapter 3. On the receiver side, the original bit sequence can be recovered by decoding and post-processing. We will explain the transmitter and receiver more fully in the next sections.

4.1 The transmitter

The detailed block diagram of the transmitter is shown in Fig.4.2. We use 8PSK as a modulation format to map a 3-bit sequence into one symbol as indicated at location 1 in Fig.4.2. Then, the 8PSK coded pulse is encoded to intensity-modulated patterns based on our previously reported 8PSK label recongnition circuit (8PRC) [31] as indicated at locations 2 and 3. Each of the encoded pulses is converted to the corresponding LG mode by SLM as indicated at location 4. Finally, they are combined and transmitted as at location 5. We will illustrate components of transmitter side in next subsections.

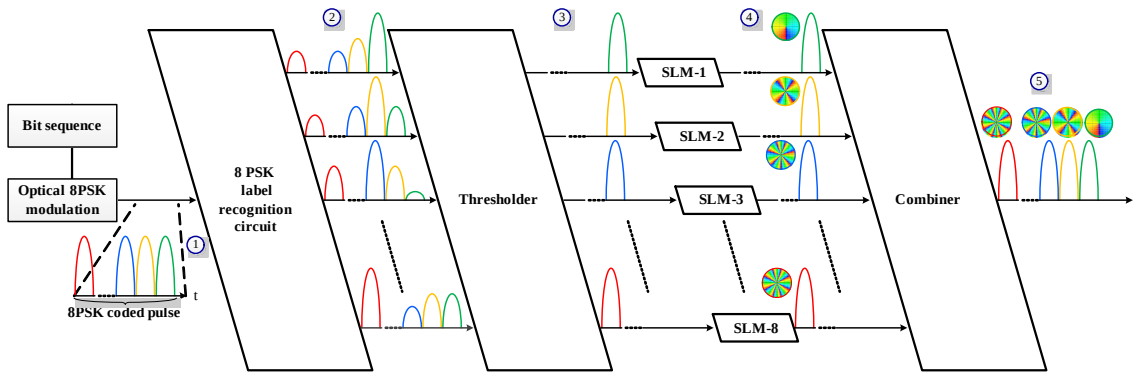

Figure 4.2: The specific structure of the transmitter

4.1.1 8PSK label recognition circuit and thresholder

A schematical diagram of the optical processing for label recognition is illustrated in Fig.4.3. We assume that an extracted optical label from an incident packet to the router is a time-series pulse train including a reference pulse. The reference pulse plays a role to identify

the phase of labels. After the preprocessing with serial-to-parallel converter [32], the parallel

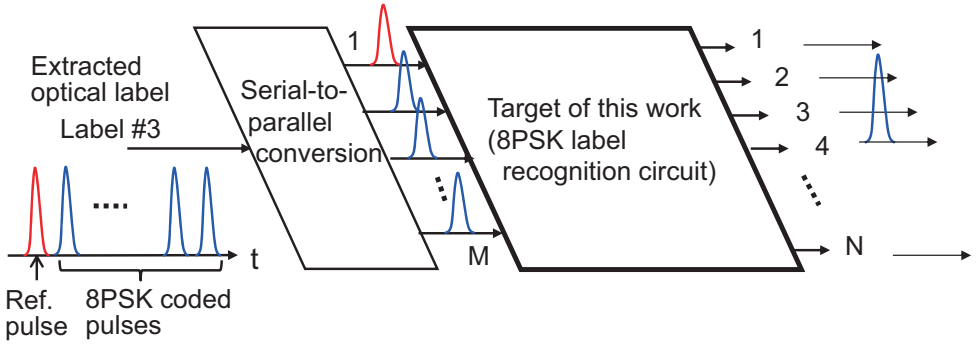

Figure 4.3: Optical processing with a label recognition circuit.

pulses are incident into the label recognition circuit. The number of output ports N is assumed to be equal to the number of labels to be recognized. The incident label is identified as the output port number having the maximum or minimum optical intensity. The serial-to-parallel conversion might not be necessary when time gates or appropriate thresholding devices are employed at the output ports in post-processing [33]. At this time, we focus on the label recognition circuit after serial-to-parallel conversion for simplicity. Our proposed 8PSK recognition circuit (8PRC) consists of two QPRCs, two Y-branches, and a phase shifter as shown in Fig.4.4. A red-colored section in Fig 4.4 shows the main structure of the basic optical waveguide circuit module of QPRC which is proposed for recognition of QPSK labels. This circuit consists of a 3-dB directional coupler, two Y-branches, and an asymmetric X-junction coupler. The combination of the transmission characteristics of these basic components with a reference signal in one of the inputs is used to recognize the phase of incident QPSK signals. In this circuit, we have 2-input and 4-output signals. The input and output relation can be

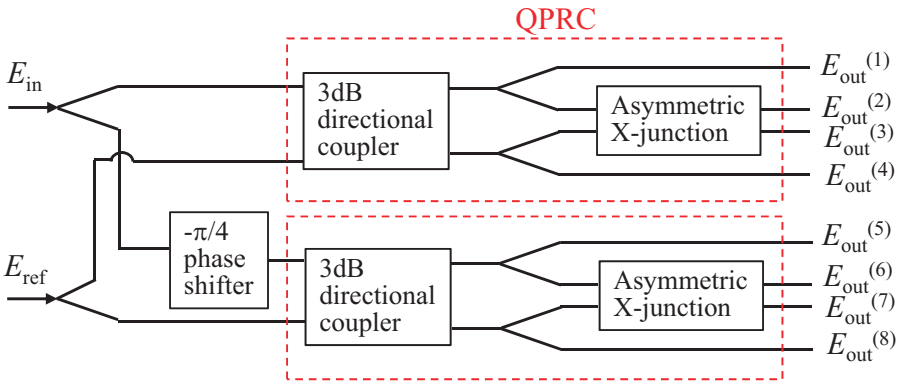

Figure 4.4: Proposed integrated-optic circuit for recognition of 8PSK coded labels.

written as [33, 34]:

$$\begin{pmatrix} E_{\text{out}}^{(1)} \\ E_{\text{out}}^{(2)} \\ E_{\text{out}}^{(3)} \\ E_{\text{out}}^{(4)} \end{pmatrix} = A_{\text{QPRC}} \begin{pmatrix} E_{\text{in}}^{(1)} \\ E_{\text{in}}^{(2)} \end{pmatrix}, \tag{4.1}$$

where

$$A_{\text{QPRC}} = \frac{1}{2} \begin{pmatrix} 1 & e^{j3\pi/2} \\ e^{j7\pi/4} & e^{j7\pi/4} \\ e^{j5\pi/4} & e^{j\pi/4} \\ e^{j3\pi 2} & 1 \end{pmatrix}. \tag{4.2}$$

From these equations, it is found that each QPSK signal at $E_{\text{in}}^{(1)}$ with a reference pulse at $E_{\text{in}}^{(2)}$ produces the maximum and null output optical intensity at a different output port corresponding to the phase of the incident signal. This function is similar to an optical 90° hybrid module [35, 36].

A $(-\pi/4)$-phase shifter is introduced to identify all of the phase values of given 8PSK coded signals. The 8PSK recognition circuit has 2-inputs and 8-output ports. We consider an input 8PSK signal as E_{in} given by

$$E_{\text{in}} = E_0 e^{jn\pi/4}, \;\; (n = 0, 1, \ldots, 7), \tag{4.3}$$

and a reference signal E_{ref} as given by

$$E_{\text{ref}} = E_0. \tag{4.4}$$

The output optical fields from the recognition circuit are related to the input signals as:

$$\begin{aligned} \begin{pmatrix} E_{\text{out}}^{(1)} \\ \vdots \\ E_{\text{out}}^{(8)} \end{pmatrix} = A_{\text{8PRC}} \begin{pmatrix} E_{\text{out}}^{(1)} \\ \vdots \\ E_{\text{out}}^{(8)} \end{pmatrix} &= \begin{pmatrix} A_{\text{QPRC}} & 0 \\ 0 & A_{\text{QPRC}} \end{pmatrix} \begin{pmatrix} \frac{1}{\sqrt{2}} & 0 \\ 0 & \frac{1}{\sqrt{2}} \\ \frac{e^{-j\pi/4}}{\sqrt{2}} & 0 \\ 0 & \frac{1}{\sqrt{2}} \end{pmatrix} \begin{pmatrix} E_{\text{in}} \\ E_{\text{ref}} \end{pmatrix} \\ &= \frac{E_0}{2\sqrt{2}} \begin{pmatrix} e^{j\pi n/4} + e^{j3\pi/2} \\ e^{j(7+n)\pi/4} + e^{j7\pi/4} \\ e^{j(5+n)\pi/4} + e^{j\pi/4} \\ e^{j(6+n)\pi/4} + 1 \\ e^{j(n-1)\pi/4} + e^{j3\pi/2} \\ e^{j(6+n)\pi/4} + e^{j7\pi/4} \\ e^{j(4+n)\pi/4} + e^{j\pi/4} \\ e^{j(5+n)\pi/4} + 1 \end{pmatrix}. \end{aligned} \tag{4.5}$$

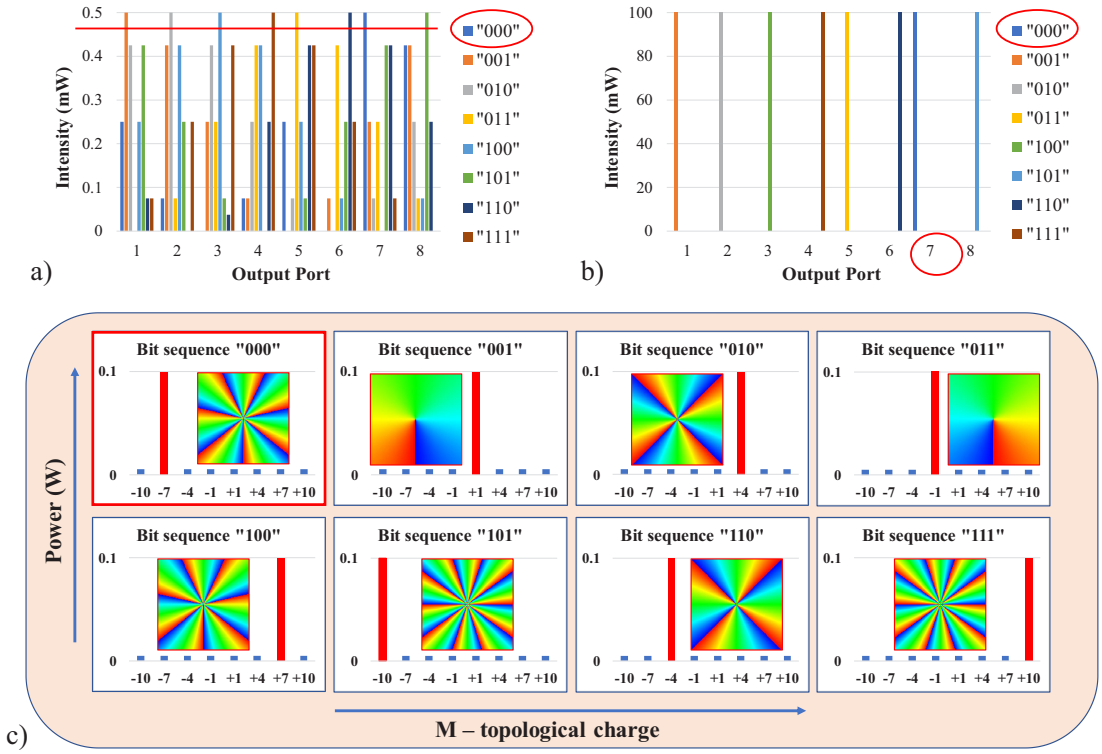

Figure 4.5: Relative output intensities of (a) 8PRC, (b) thresholder, and (c) SLMs.

As a result of this equation, there are five different optical intensities at each of the output ports. Fig.4.5a shows the theoretical relative output intensities $|E_{\text{out}}^{(k)}/E_0|^2$ for eight codes. It is found that one output port has the maximum intensity for each 8PSK code. Besides, one output port has a minimum (null) intensity for each 8PSK code. The maximum and the minimum intensities are 0.5mW and 0mW, respectively. The second maximum intensity of 0.427mW (85.4 % of the maximum intensity) appears at two output ports. The second minimum intensity of 0.073mW (14.6 % of the maximum intensity) appears also at two output ports. Two recognition schemes are considered according to this theoretical calculation, i.e., the maximum or minimum output port is used to determine the thresholding level. In other words, a threshold processing is performed at the intensity between the maximum and the second maximum intensities to identify the phase of the 8PSK coded labels in the maximum-output scheme. Similarly, the threshold processing is performed at the intensity between the minimum and the second minimum intensities in the minimum-output scheme.

4.1.2 The Spatial light modulator (SLM)

A spatial ligh modulator is one key module that is used for controlling light in two dimension including an address part and a light modulation part. A SLM modulates the intensity and phase of the light beam by the changing informartion of these 2 parts. In our research, 8 different SLMs are used to generate Laguerre-Gaussian beams where TCs are $m_1 = -10$, $m_2 = -7$, $m_3 = -4$, $m_4 = -1$, $m_5 = +1$, $m_6 = +4$, $m_7 = +7$, and $m_8 = +10$. Intensity and phase profiles of these 8LG beams are shown in Fig.4.6.

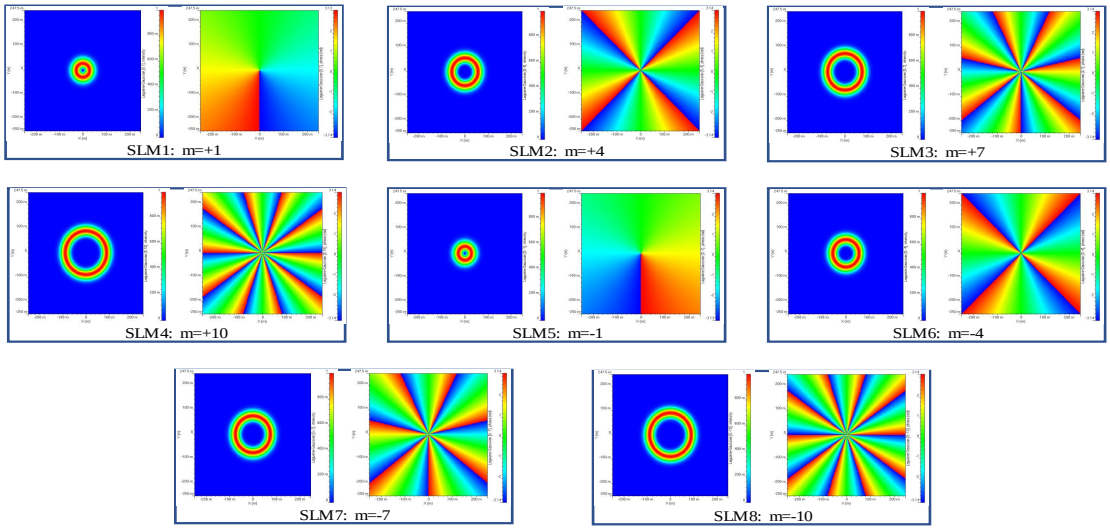

Figure 4.6: Intensity and phase profiles of SLMs

4.1.3 Combiner

A combiner that implements parallel to serial conversion is the last key component in conversion between 8PSK and 8OAM. Modes that can indicate transmitted bit sequence at individual time slots are combined and a series of OAM beams are generated by this component. In other words, the full 8-ary OAM-SK modulation is completed at the output of the combiner.

The full 8-ary OAM-SK can be explained from the Fig.4.5. For example in Fig.4.5(a), when the transmitted optical intensity is 1 mW and bit sequence is '000', the highest output intensity of 0.5 mW comes at output port #7 and the 2nd highest intensity of 0.42 mW comes at output port #8.

By putting a threshold level between these two intensities, namely at 0.46mW, the output of the threshold becomes high-level at 100 mW for the maximum output and low-level for the other outputs as shown in Fig.4.5(b). Thus, there is only one port having a high-level output

depending on the bit sequence. A possible optical threshold has been reported in [37], which distinguishes low and high power levels by using nonlinear ring resonators whose resonant condition changes due to the nonlinear phase change in high signal power. The high-level output signal at each port is then converted to a corresponding OAM mode by using SLMs as shown in Fig.4.5(c).

Finally, an 8×1 combiner consisting of tree-connection beam splitters implements parallel to serial conversion with loss of 1/8 to obtain a series of the 8-ary OAM-SK (8OAM-SK) in which each of the one-symbol periods has a single OAM mode depending on the bit sequence. Fig.4.7 shows the relation between 8PSK constellation and 8OAM-SK mapping with bit sequences.

4.2 The receiver

The modulated light beam is transmitted to the receiver through the FSO link with atmospheric turbulence. The block diagram of the receiver is shown in Fig.4.8. A squared receiver optical aperture is placed to extract the incoming beam. There is an issue of the power loss at the aperture due to beam divergence in the FSO link, which we will consider in the simulation. Then, the receiver recognizes the incoming OAM mode to demodulate the bit pattern by using an OAM demutiplexing method. It is based on the inverted spiral phase mask and a spatial filter that is implemented by SLM and a pinhole-like aperture, respectively. It includes several parts including optical to electrical conversion, power comparator, and post-processing. Optical to electrical conversion circuit is used to create electrical signals from optical signals using SLMs, pinhole-like aperture, and photodetection for each corre-

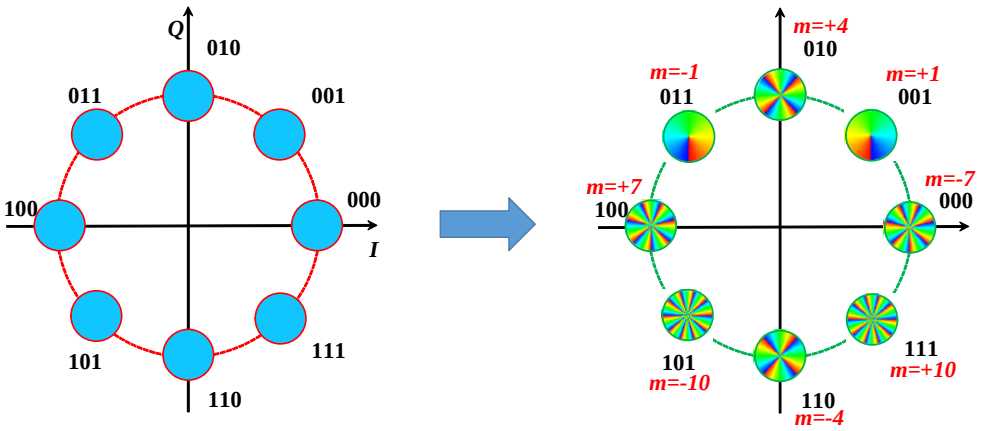

Figure 4.7: Relation between 8PSK constellation and 8OAM-SK mapping with 3-bit sequences.

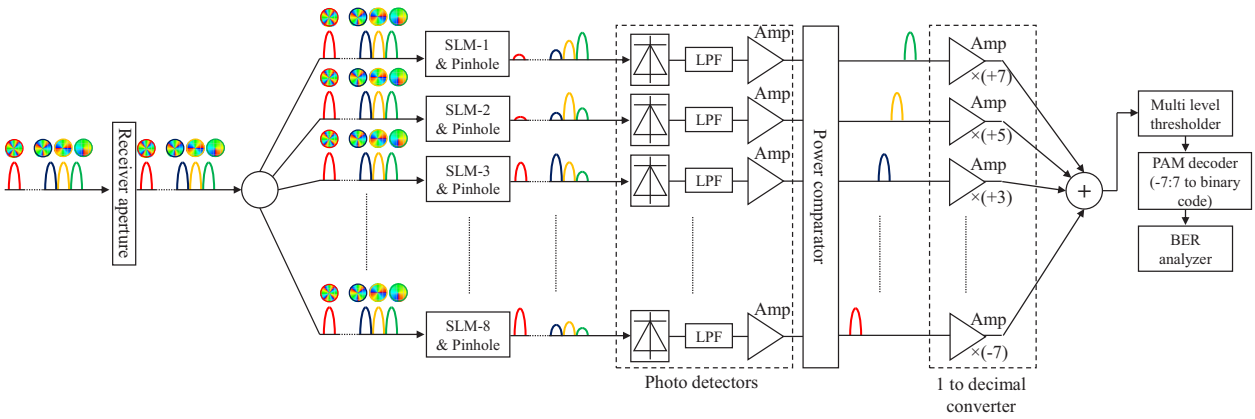

Figure 4.8: The specific structure of the receiver

sponding OAM beams at the time slot. A power comparator is used to detect which OAM mode is transmitted from the transmitter. Two kinds of comparing methods such as serial and parallel are usable in our system. Finally, the post-processing circuit with 1 to decimal converter is used to measure the BER to evaluate proposed 8-ary OAM-SK in this study.

4.2.1 Optical to electrical conversion

The beam passed through the optical aperture is then split to 8 beams with a loss of 1=8 by tree-connection beam splitters. The 8-split received beams are demodulated by using eight SLMs each of which has the inverted phase hologram compared to that in the transmitter. Then, only one of eight beams out is converted back to OAM mode with $m = 0$ in a symbol period and has a high-intensity spot at the beam center. Fig.4.9 shows this conversion.

The pinhole-like aperture extracts the high-intensity spot. The extracted power depends on the pinhole size. Fig.4.10 shows a preliminary calculation of the intensity distribution and power of the extracted OAM mode $m = 0$ with a variety of pinhole size. The shapes of the pinholes are sets of two-dimensional discrete pixels restricted to the spatial resolution of the simulation. The OAM mode $m = 0$ is assumed to have a 3.2-cm diameter and 1-mW power without the influence of turbulence. The power of 1 mW is calculated as 100 mW at the output of the threshold in the transmitter followed by SLMs with 80% efficiency, 1/8 loss at the combiner, no loss in the link and the receiver aperture, 1/8 loss at the splitter, and again SLMs with 80% efficiency in the receiver. It is found that the extracted powers are 0.034, 0.148, 0.241, and 0.311 mW for 1-, 5-, 9-, and 13-pixels. Since the power may fluctuate and differ in the turbulent condition, we will analyze the optimum pinhole size in the simulation.

Then, the photo-detector (PD) detects the intensity and it converts an optical signal to an electrical signal. The signals detected by PDs are filtered by the low pass filter (LPF)

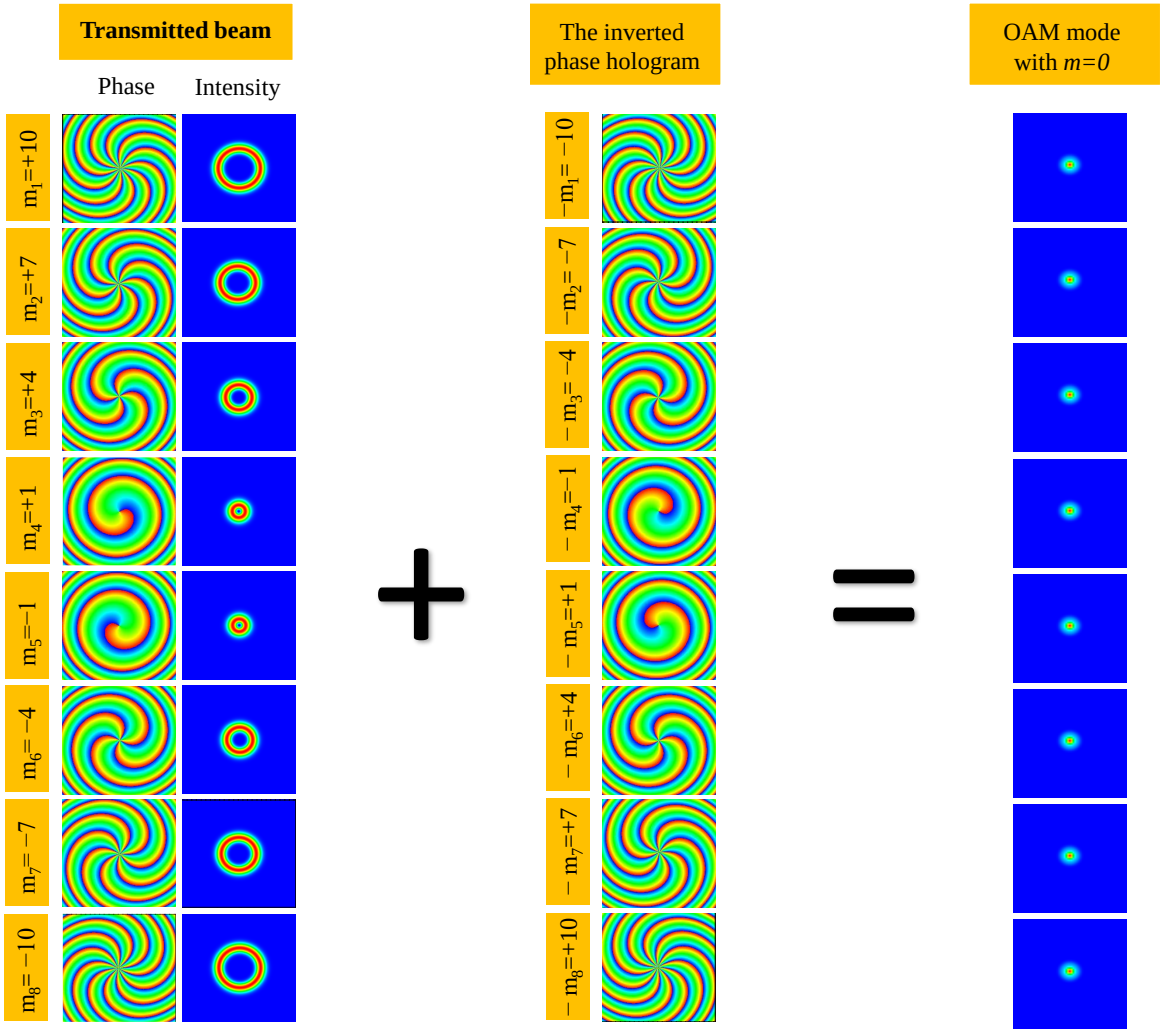

Figure 4.9: The output of the inverted phase hologram

with the cutoff frequency of the symbol rate and are amplified. The amplified electric signals are sent to the power comparator.

4.2.2 Power comparator

The power comparator finds the highest intensity from the eight signals in every symbol period. The output becomes 1 for the highest intensity and 0 for the others. Two kinds of decoding methods are investigated in our study. 1) decoding with serial comparator 2) decoding with a parallel comparator.

Decoding with serial comparator: In this method, thresholds, which have different values according to the blue colored lines in Fig.4.11, are connected to each output of SLMs. If

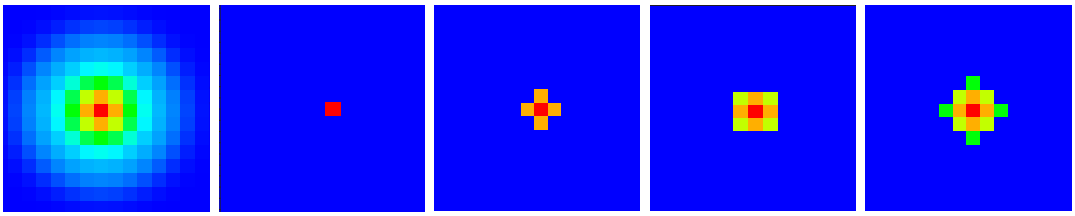

a) OAM mode with *m=0* (1.0 mW) | **b) 1 pixel aperture** (0.034 mW) | **c) 5 pixels aperture** (0.148 mW) | **d) 9 pixels aperture** (0.241 mW) | **e) 13 pixels aperture** (0.311 mW)

Figure 4.10: Some example of the pinhole-like aperture

the input of the threshold is higher than the threshold value, the output will be 1. Otherwise, the output will be 0. For example, the output of SLM-7 has the highest amplitude when transmitting LG0-7 (carrying '000' bit sequence) beam and second-highest amplitude is found when transmitting LG0-10 (carrying '101' bit sequence) beam. So, the thresholding value should be between the first and second amplitudes. The thresholding value is fixed for the system. So it faces some disadvantages such as turbulence is a random process and the first maximum amplitude becomes smaller than thresholding level when the medium has strong turbulence.

Decoding with parallel comparator: The output powers of all SLMs at the one-time slot are compared with each other. In other words, the power comparator finds the highest intensity from the eight candidates in every symbol period. For example, comparing values are shown by a red-colored ring in Fig.4.11 when transmitting LG0-7 (carrying '000' bit sequence) beam. Maximum power is detected in SLM-7. So, the system sets that the 7th output of power comparator is 1, other outputs are 0 value. As a result, the system decodes that transferred information is '000'.

4.2.3 Post processing

The bit sequence is retrieved by the following circuits including 1 to decimal converters, an adder, a multi-level threshold, and a pulse amplitude modulation (PAM) decoder. The 1 to decimal converters are parallel eight amplifiers with different gains of 7, 5, 3, 1, -1, -3, -5, and -7 from the top port to the bottom port to generate amplitude different signals from the output of the power comparator depending on the port number. The multi-level threshold converts the amplitude different signals to binary-compatible multi-level signals that are internally used in the simulation software. Then, the PAM decoder converts the multi-level signals into a bit sequence. The retrieved bit sequence is compared with the original bit sequence to measure BER by the BER analyzer. Note that the implementation

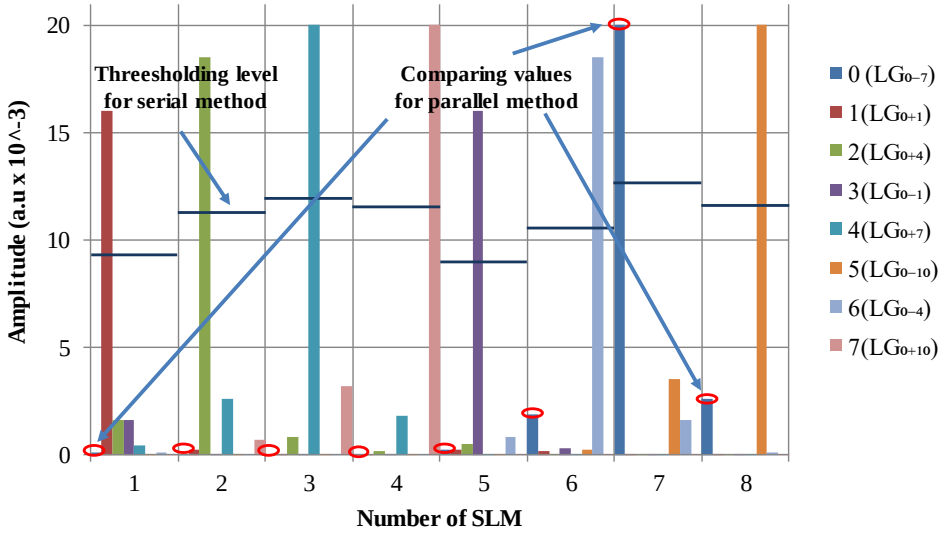

Figure 4.11: The input of power comporator

of the 1 to decimal converters and the following components is an instance of the bit sequence demodulation for our numerical simulation. Other implementations such as offline processing with the recorded signals [8], [9] can be candidates for the data recovery.

Chapter 5

Simulation and results

The proposed 8OAM-SK method is implemented on the OptiSystem software (Optiwave Systems inc.). Representative physical and numerical parameters are listed in Table 5.1. In our study, we simulated 8-OAM Shift Keying for the FSO communication system for two kinds of phenomena. The first one is phase distortion due to atmospheric turbulence on the 1000m FSO link. The second one is background noise and scintillation effect due to atmospheric turbulence on the 1000m FSO link. In this chapter, we illustrate our simulation process and simulation results on these two phenomena.

5.1 Phase distortion due to atmospheric turbulence on 8OAM-SK for FSO communication

The concept of 8OAM-SK is explained in chapter 4. The specific structure of the transmitter is shown in Fig.4.2. We used the 8PSK recognition circuit to generate 8 labeled intensity from the original 8PSK signal in the transmitter. The time-domain of the output of 8PSK-RC at location 2 of Fig.4.2 is shown in Fig.5.1. Maximum and second maximum intensities are found at around 7.9mW and 6.7mW, respectively. It is 2.9mW and 2.5mW higher than the theoretical calculation. We set thresholding levels at an average of maximum and second maximum intensities (7.3mW). Then, each output connects into corresponded SLMs and these 8 different OAM beams are mixed by the combiner as mentioned in chapter 4.1. Time domain after combiner at location 5 of Fig.4.2 is shown in Fig.5.2.

Fig.5.3 shows some examples of the intensity and phase profiles of the eight OAM modes after transmitted through atmospheric turbulence (without turbulence, weak turbulence ($C_n^2 = 1 \times 10^{-15}$ m$^{-2/3}$), strong turbulence ($C_n^2 = 1 \times 10^{-14}$ m$^{-2/3}$)). It is found that the transmitted beam is strongly distorted by the strong turbulence.

To reveal the issue of the power loss at the receiver optical aperture in the FSO link,

Table 5.1: List of parameters

Parameters	Value
Bit rate	30, 60, 120 Gbps
Frequency	193.1 THz
Polarization	Linear (X axis)
OAM modes (LG0m)	m_8=−10 (bit symbol '101'), m_7 =−7 (bit symbol '000'), m_6 =−4 (bit symbol '110'), m_5 =−1 (bit symbol '011'), m_4 =+1 (bit symbol '001'), m_3 =+4 (bit symbol '010'), m_2 =+7 (bit symbol '100'), m_1 =+10 (bit symbol '111')
Turbulence strength (C_n^2)	From 1×10^{-15} to 1.75×10^{-14} $m^{-2/3}$
Inner scale (l_0)	1 mm
Outer scale (L_0)	100 m
Propagation distance	1000 m
Size of phase screen	0.5×0.5 m
Number of grid	200×200

Fig.5.4 shows the relation between the size of the squared optical aperture and the power loss in the case of 120-Gbps data rate and 3-cm beam waist. There is no turbulence in this calculation. As one can estimate from the intensity profile in Fig.5.3, beams with bigger TC require bigger aperture size to accommodate the whole beam without loss. Thus, we choose 30-cm aperture size to collect the whole of the beam of $m = \pm 10$ which is the maximum number of TC in the analysis. Although a spot size converter (a combination of lenses) should practically be employed to fit the beam size to following optical components, we do not use it in our simulation since our numerical calculation has the limited spatial resolution of 2.5 mm/pixel due to the memory restriction of the computer. Partial information of the distortion on the beam after turbulent link propagation will be lost if we introduce a spot size converter and shrink the beam diameter below 10 mm which is the typical screen size of

commercially available SLMs.

Fig.5.5 shows the intensity profiles after the SLMs in the receiver for all combinations of the transmitted OAM modes on the top header and the displayed inverse phase mask on the receiver SLMs on the left-side header. The turbulence strength is set as $C_n^2 = 1 \times 10^{-15}$ $\mathrm{m}^{-2/3}$. There is a bright spot at the beam center when the transmitted OAM mode is correctly demodulated by the corresponding inverted spiral phase as shown in the diagonal (a1, b2, ..., h8) of Fig5.5. Otherwise, the demodulated beams have doughnut shapes with a vacant central spot. Then, the receiver aperture extracts the correctly demodulated bright central spot.

Next, we determine the optimum pinhole aperture size for 4 cases where apertures are 1, 5, 9, and 13 pixels shown in Fig.4.10. The shapes of the pinhole apertures are indicated near the curves. The transmitted beam waist is 3 cm and the turbulence strength is $C_n^2 = 1 \times 10^{-14}\mathrm{m}^{-2/3}$. The data rate is set as 120 Gbps. Fig.5.6 shows the time domain after each SLMs and pinhole aperture for each pinhole aperture size. Crosstalk between modes is fluctuated due to the strength of the turbulence. One of reduction method is the

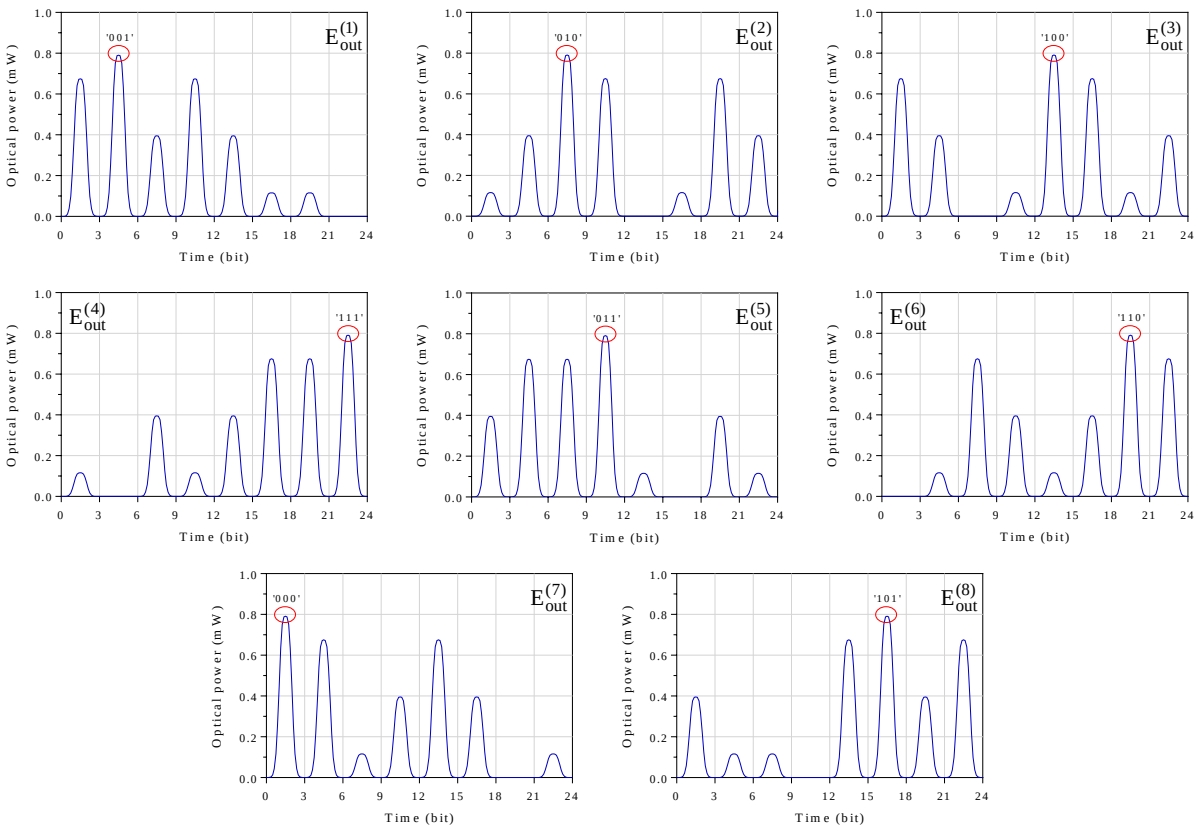

Figure 5.1: Time domain of output of 8PSK-RC at transmitter

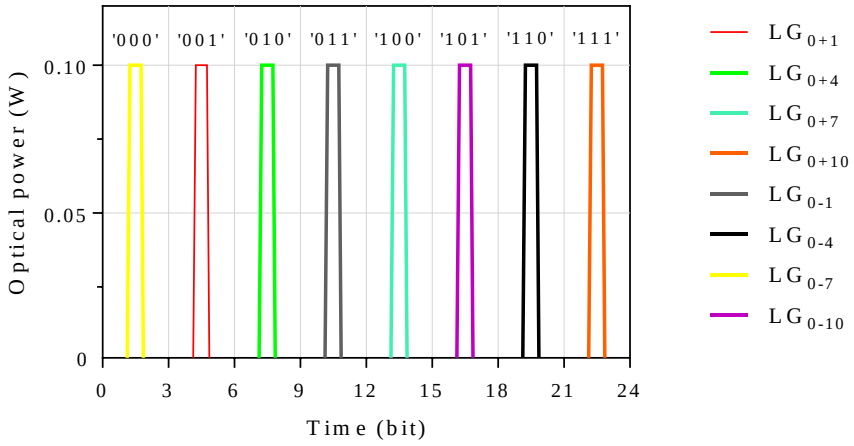

Figure 5.2: Time domain of after combiner at transmitter

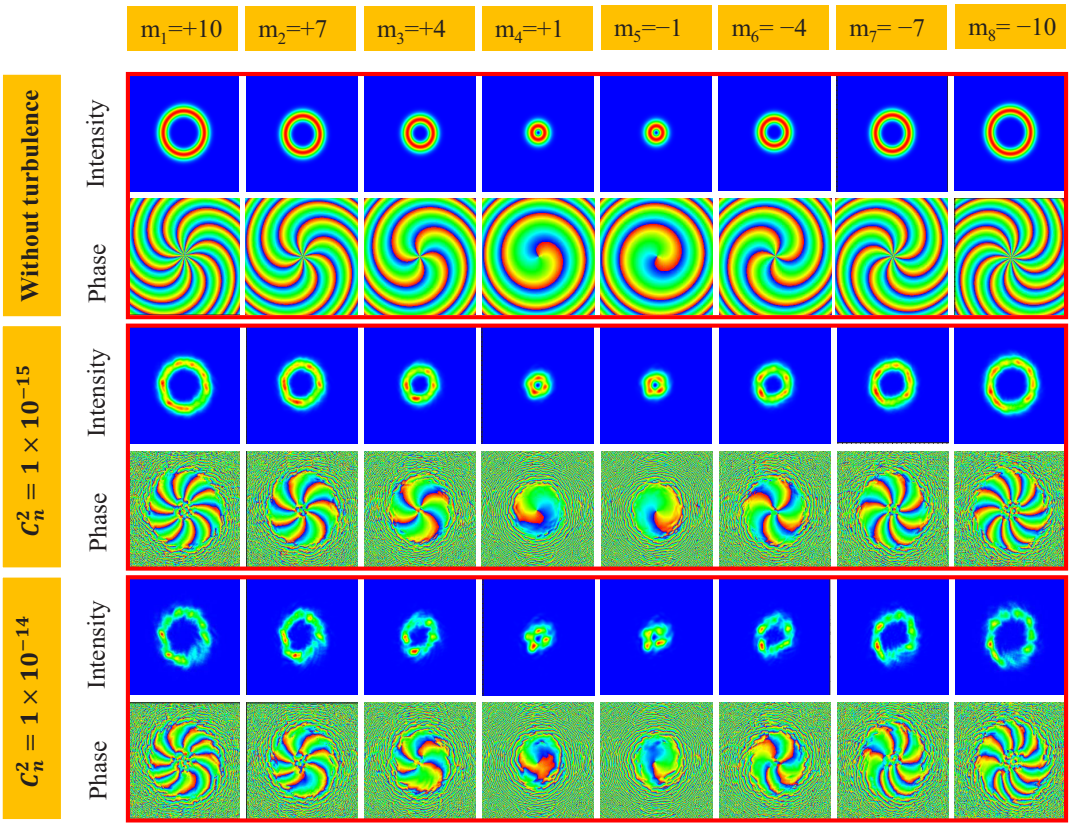

Figure 5.3: The intensity and phase profile after transmitted through the atmospheric turbulence

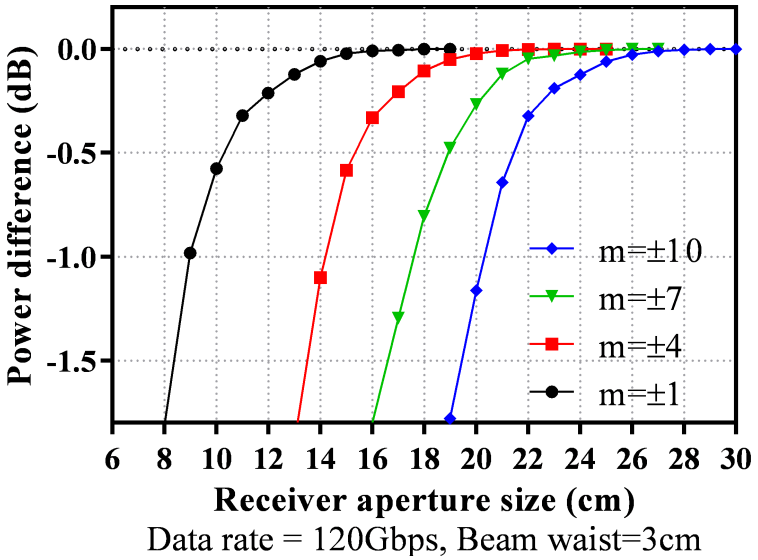

Figure 5.4: The relation between receiver aperture size and power

optimization of pinhole aperture size. Bigger pinhole size is suitable to truncate full intensity from received OAM beam. However, crosstalk between detected OAM modes from received OAM beam is increased when pinhole size is non-optimum. In our research, we use the parallel comparator which detects maximum intensity from eight candidates in every timeslot. Maximum intensities at first timeslot where the transmitted mode is LG_{0+7} which carrying '000' bit sequence are found at seventh SLM and pinhole (inverse phase mask mode is -7). Its value is 2.25, 1.79, 1.08, and 0.26mW for 13, 9, 5, and 1pixel aperture, respectively as shown in seventh row of Fig.5.6. The second maximum intensities at the same timeslot are found at sixth SLM and pinhole (inverse mask mode is -4). Its value is 1.37, 0.9, 0.531, and 0.113mW for 13, 9, 5, and 1 pixel aperture, respectively as shown in sixth row of Fig.5.6. It is around 60.8, 50.27, 49.16, and 43.46 percent of maximum intensity at the same timeslot.

Fig5.7 shows the BER performance as a function of the received power with the pinhole aperture size as a parameter. The received power is measured after the receiver SLM and before the pinhole aperture. Crosstalk is lower at the 1-pixel aperture as a result in Fig.5.6 but good BER performance is found that the left-most 9-pixels result effectively detects the focused power in the bright spot. Therefore, the 9-pixels aperture is used in the simulation.

Then, we evaluate the BER performance as a function of the received power with the turbulence strength as a parameter as shown in Fig.5.8. The data rate and symbol rate are set as 120 Gbps and 40 GBaud, respectively. The turbulence strength C_n^2 is from 1×10^{-14} $\mathrm{m}^{-2/3}$ to 1.75×10^{-14} $\mathrm{m}^{-2/3}$ as shown in the legend of Fig.5.8.

Note that each BER value is calculated by avaraging the six results with randomly generated different phase screens. It is found from Fig.5.8 that the received power to ob-

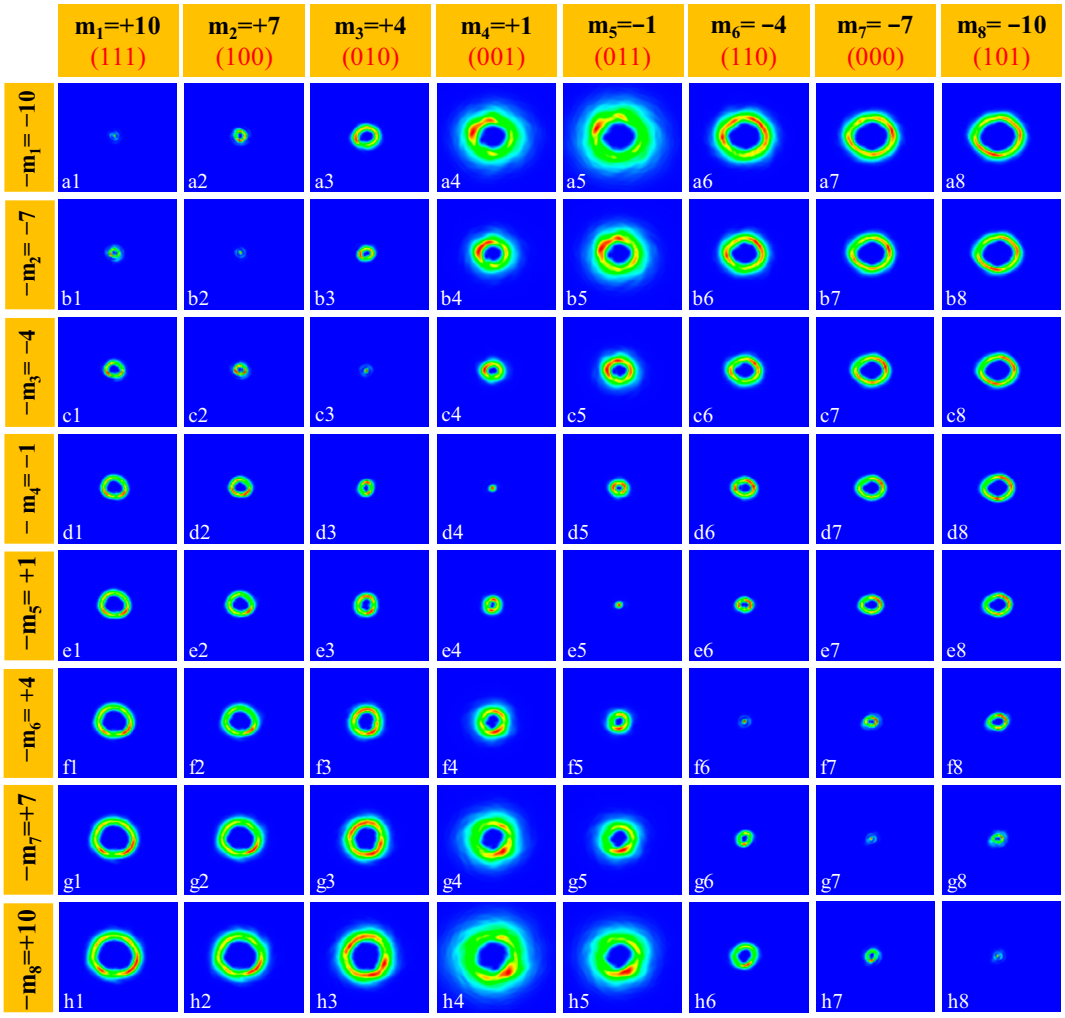

Figure 5.5: All possible intensity profile of 8OAM-SK after demodulation under turbulence with $C_n^2 = 1 \times 10^{-15} \mathrm{m}^{-2/3}$

tain the same BER value becomes higher when the turbulence strength becomes stronger. There is a solid line of 7% overhead hard-decision forward error corretion (FEC) limit at $\log_{10}(3 \times 10^{-8}) = -2.42$ in Fig.5.8. The error free transmission is expected for BER below the FEC limit. The power penalties compared to the result of $C_n^2 = 1 \times 10^{-14}$ $\mathrm{m}^{-2/3}$ on the FEC limit are 3, 7 and 17dB for turbulence strength of $C_n^2 = 1.25 \times 10^{-14}$ $\mathrm{m}^{-2/3}$, $C_n^2 = 1.5 \times 10^{-14}$ $\mathrm{m}^{-2/3}$ and $C_n^2 = 1.75 \times 10^{-14}$ $\mathrm{m}^{-2/3}$, respectively. BER performance as a function of the C_n^2 with different data rate and received power is shown in Fig5.9. It is found that the acceptable turbulence strength to obtain the same BER value becomes weaker when the data rate becomes higher. Also, the higher received power has a stronger tolerance for turbulence. The C_n^2 difference between the different data rate to obtain the same BER is

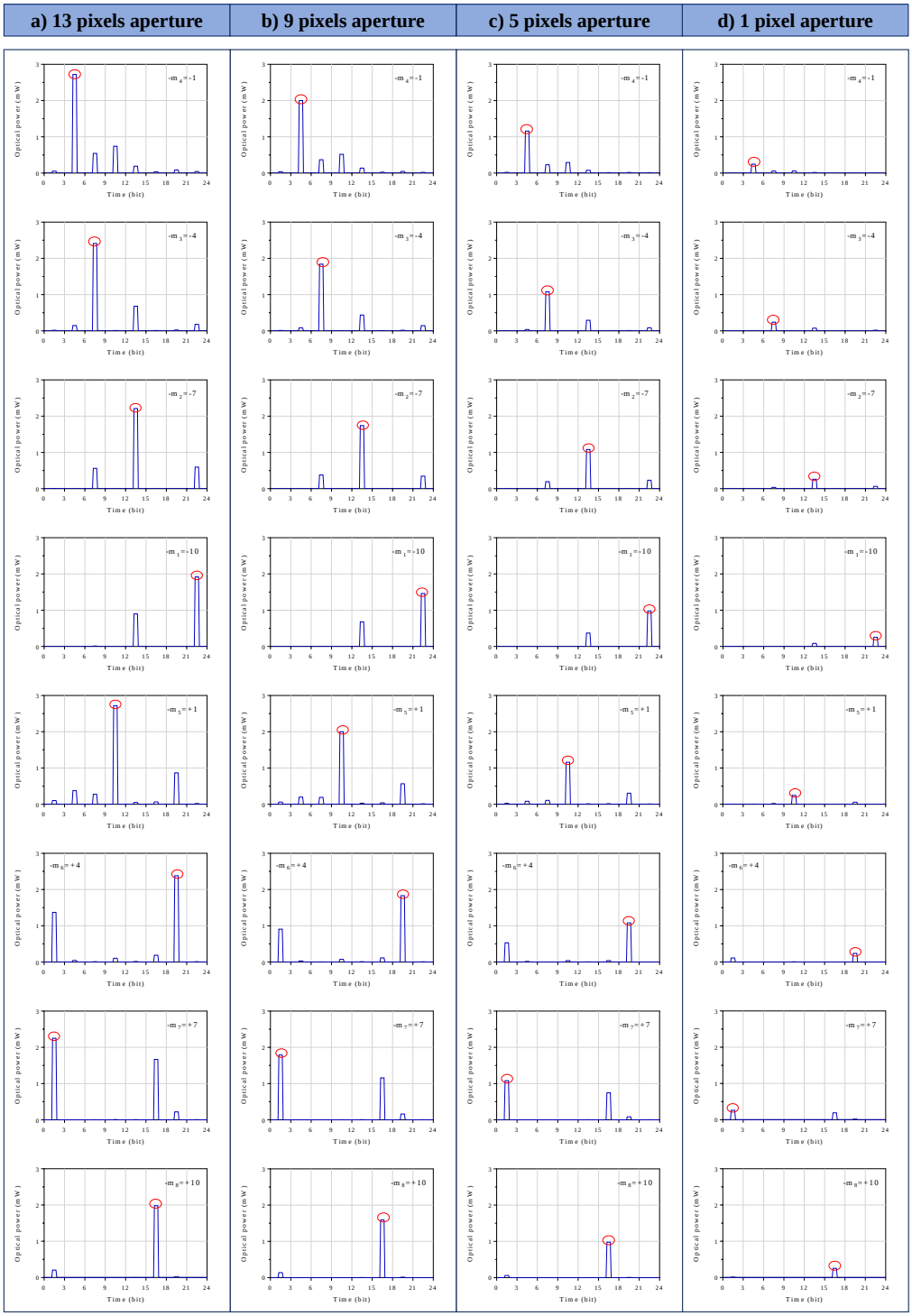

Figure 5.6: Time domain after SLM and pinhole aperture in receiver

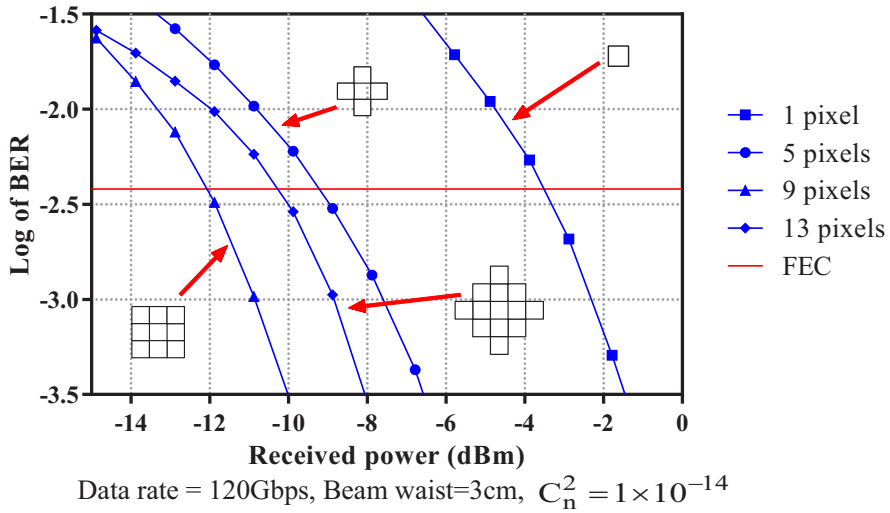

Figure 5.7: BER performance as a function of received power with pinhole aperture size as a parameter.

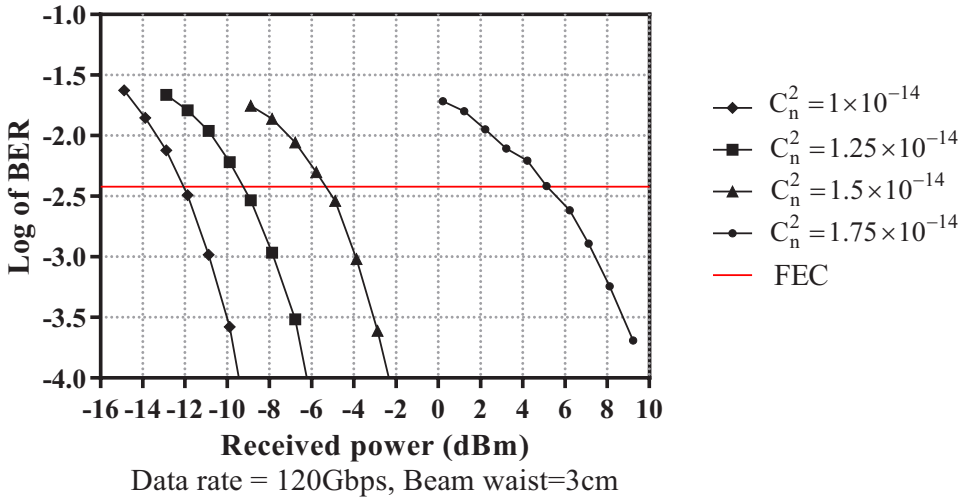

Figure 5.8: BER as a function of received power for 8OAM-SK-FSO communication system with turbulence strength as a parameter.

smaller for the high-power result.

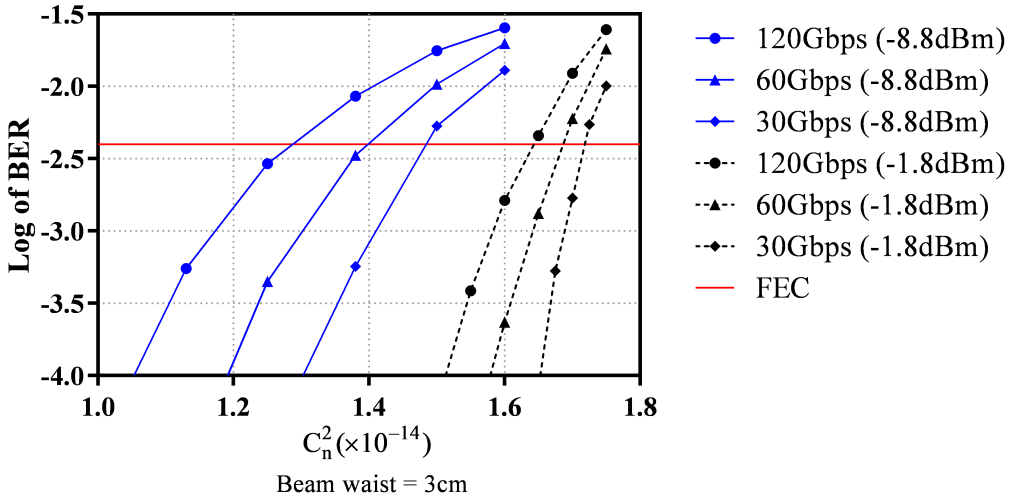

Figure 5.9: BER as a function of C_n^2 for 8OAM-SK-FSO communication system with data rate and received power as parameters.

5.2 Background noise and scintillation effect due to atmospheric turbulence on 8OAM-SK for FSO communication

In this section, we implemented a simulation for the scintillation effect due to atmospheric turbulence in our proposed 8OAM-SK system. The simulation set up is illustrated in Fig.5.10.

In this simulation, the bit rate is 30Gbps with a symbol rate of 10Gbps and. The simulation setup is almost the same as the previously mentioned 8OAM-SK system but it has several differences. 1: after the thresholding, amplified spontaneous emission (ASE) noise is added by the SetOSNR module to evaluate bit error performance due to background noise. 2: We used an ideal mode selector at the receiver side. It does not include an inverse phase mask and pinhole like aperture. 3: FSO communication link does not include a phase screen. In other words, phase distortion due to atmospheric turbulence is not analyzed and the system does not have any crosstalk between used Laguerre-Gaussian model. Each output signal of 8PSK-RC is converted to different 8 OAM modes. Then it is combined and transferred through the FSO link with a 1 km link range. We use the FSO link model with Gamma-Gamma distribution which is mentioned in chapter 2. We use eight different Laguerre-Gaussian (LG) modes. Only one mode is transferred at a one-time slot. The post-processing circuit includes photodiodes, low pass filters, electrical amplifiers and thresholds on the receiver side. in this simulation, we used serial comparator. So, one of the important

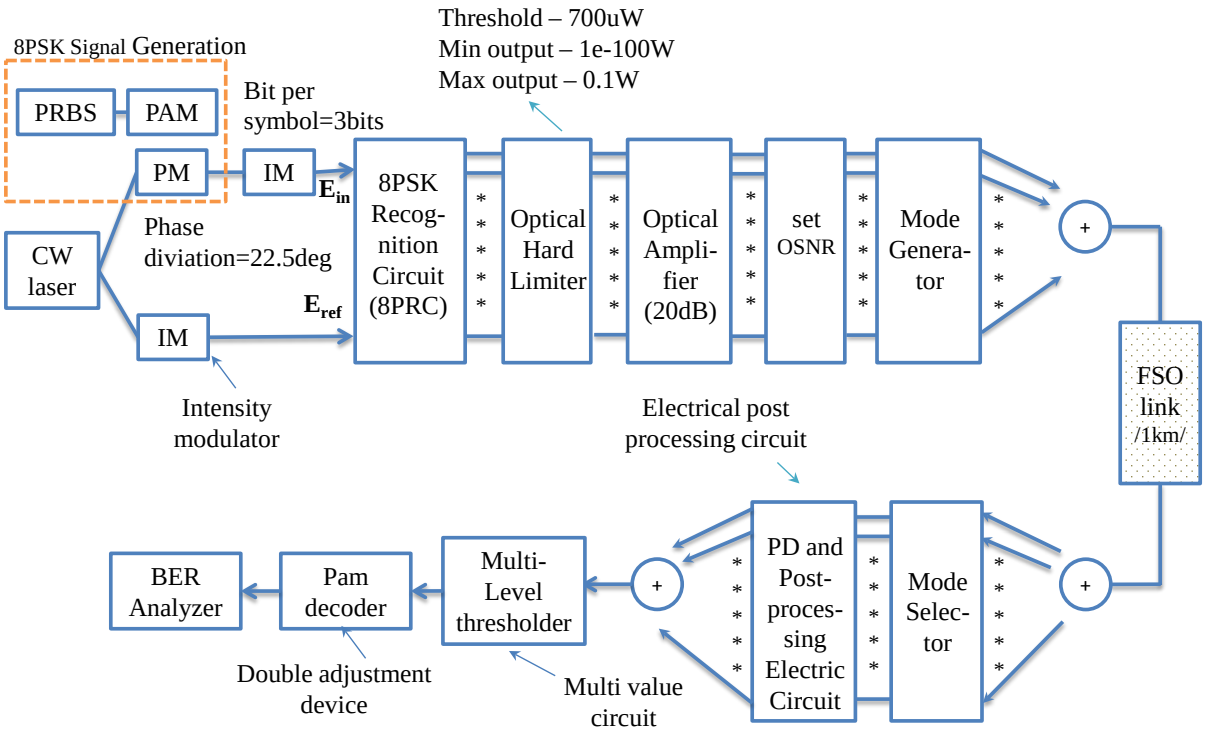

Figure 5.10: Schematic of the proposed circuit for the scintillation effect due to atmospheric turbulence.

configurations is the threshold value of the post-processing circuit. The threshold converts the signal into 1 or 0 depending on whether the intensity of the received signal is higher or lower than its thresholding value. We set different values of the threshold depending on the atmospheric attenuation.

The simulated bit-error-rate (BER) performance at Att_{atm} =5dB/km and 15dB/km in FSO are shown in Fig.5.11 and Fig.5.12, respectively. To evaluate the simulation result, we compare it with a case where an 8PSK signal is received by a coherent receiver instead of 8PRC. As shown in Fig.5.11, required OSNRs for 7% overhead hard-decision forward error correction (FEC) limit of $\log_{10}(3.8 \times 10^{-3}) = -2.42$ are around 6.3dB and 11.3dB for the proposed circuit and the coherent circuit, respectively at moderate turbulence $C_n^2 = 10^{-14}$. OSNRs at the FEC limit is 5dB smaller than the coherent circuit. Similar characteristics are observed at different value of C_n^2 in Fig.5.11 . The reason for BER floors for $C_n^2 = 10^{-13}$ and 5×10^{-13} is due to the increased attenuation of scintillation. The threshold value in the receiver was kept as a fixed value even when C_n^2 was changed. Thus, the threshold value became not suitable for the BER decision. It is observed from Fig.5.12 that the BER performances of the proposed circuit have almost 0.6-dB right-shift values compared to those of Fig.5.11 . In contrast, the results of the coherent circuit have 2- to 4-dB right-shift values

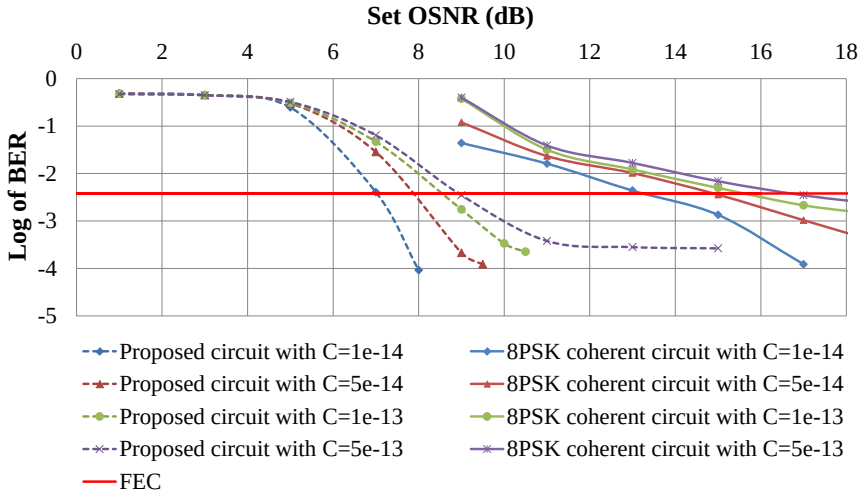

Figure 5.11: BER performance at Att_{atm} =5dB/km.

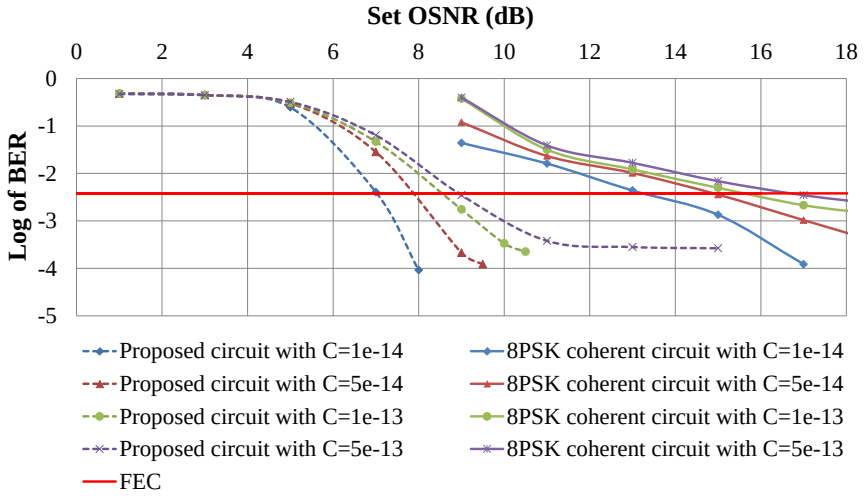

Figure 5.12: BER performance at Att_{atm} =15dB/km.

compared to Fig.5.11 . Also, stretched BER range on the FEC limit compared to Fig.5.11 is observed. Therefore, we can conclude that the proposed circuit has a stronger tolerance to the attenuation in the FSO channel.

Chapter 6

Conclusion

In this study, we have proposed the 8OAM-SK-FSO communication system in which the original bit information is encoded and modulated from the 8PSK signal into 8-ary OAM states. As a result of the several BER performance investigations, we revealed that the receiver aperture size was one of the important parameters to improve the transmission signal quality by effectively collecting the received power. It was also found that higher received power was required in stronger turbulence to achieve acceptable signal quality. Also, the lower data rate showed better tolerance to the turbulence strength.

In our future works, we will consider employing a compensation method for the intensity and phase fluctuation caused by the turbulence to further improve the tolerance and BER performance. Experimental verification is also included in future works.

References

[1] V. M. Research, "Free space optics market," *Market Research Report*, 2017.

[2] L. Allen, M. W. Beijersbergen, R. Spreeuw, and J. Woerdman, "Orbital angular momentum of light and the transformation of laguerre-gaussian laser modes," *Physical Review A*, vol. 45, no. 11, p. 8185, 1992.

[3] Y. Liu, Y. Ke, J. Zhou, Y. Liu, H. Luo, S. Wen, and D. Fan, "Generation of perfect vortex and vector beams based on pancharatnam-berry phase elements," *Scientific reports*, vol. 7, p. 44096, 2017.

[4] S. Orlov and A. Stabinis, "Free-space propagation of light field created by bessel–gauss and laguerre–gauss singular beams," *Optics communications*, vol. 226, no. 1-6, pp. 97–105, 2003.

[5] H. Huang, G. Xie, Y. Yan, N. Ahmed, Y. Ren, Y. Yue, D. Rogawski, M. J. Willner, B. I. Erkmen, K. M. Birnbaum *et al.*, "100 tbit/s free-space data link enabled by three-dimensional multiplexing of orbital angular momentum, polarization, and wavelength," *Optics letters*, vol. 39, no. 2, pp. 197–200, 2014.

[6] Q. Tian, L. Zhu, Y. Wang, Q. Zhang, B. Liu, and X. Xin, "The propagation properties of a longitudinal orbital angular momentum multiplexing system in atmospheric turbulence," *IEEE Photonics Journal*, vol. 10, no. 1, pp. 1–16, 2018.

[7] G. Gibson, J. Courtial, M. J. Padgett, M. Vasnetsov, V. Pas' ko, S. M. Barnett, and S. Franke-Arnold, "Free-space information transfer using light beams carrying orbital angular momentum," *Optics express*, vol. 12, no. 22, pp. 5448–5456, 2004.

[8] C. Kai, P. Huang, F. Shen, H. Zhou, and Z. Guo, "Orbital angular momentum shift keying based optical communication system," *IEEE Photonics Journal*, vol. 9, no. 2, pp. 1–10, 2017.

[9] W. Wang, P. Wang, T. Cao, H. Tian, Y. Zhang, and L. Guo, "Performance investigation of underwater wireless optical communication system using m-ary oamsk modulation over oceanic turbulence," *IEEE Photonics Journal*, vol. 9, no. 5, pp. 1–15, 2017.

[10] I. B. Djordjevic, "Deep-space and near-earth optical communications by coded orbital angular momentum (oam) modulation," *Optics express*, vol. 19, no. 15, pp. 14 277–14 289, 2011.

[11] Q. Tian, Z. Li, K. Hu, L. Zhu, X. Pan, Q. Zhang, Y. Wang, F. Tian, X. Yin, and X. Xin, "Turbo-coded 16-ary oam shift keying fso communication system combining the cnn-based adaptive demodulator," *Optics express*, vol. 26, no. 21, pp. 27 849–27 864, 2018.

[12] A. E. Willner, H. Huang, Y. Yan, Y. Ren, N. Ahmed, G. Xie, C. Bao, L. Li, Y. Cao, Z. Zhao *et al.*, "Optical communications using orbital angular momentum beams," *Advances in Optics and Photonics*, vol. 7, no. 1, pp. 66–106, 2015.

[13] H. Kaushal and G. Kaddoum, "Free space optical communication: challenges and mitigation techniques," *arXiv preprint arXiv:1506.04836*, 2015.

[14] H. Kaushal, V. Jain, and S. Kar, *Free space optical communication*. Springer, 2017, vol. 18.

[15] A. K. Majumdar and J. C. Ricklin, *Free-space laser communications: principles and advances*. Springer Science & Business Media, 2010, vol. 2.

[16] M. Uysal, C. Capsoni, Z. Ghassemlooy, A. Boucouvalas, and E. Udvary, *Optical wireless communications: an emerging technology*. Springer, 2016.

[17] M. Khatib, *Contemporary issues in wireless communications*. BoD–Books on Demand, 2014.

[18] P. Vaity and L. Rusch, "Perfect vortex beam: Fourier transformation of a bessel beam," *Optics letters*, vol. 40, no. 4, pp. 597–600, 2015.

[19] J. A. Anguita, M. A. Neifeld, and B. V. Vasic, "Turbulence-induced channel crosstalk in an orbital angular momentum-multiplexed free-space optical link," *Applied optics*, vol. 47, no. 13, pp. 2414–2429, 2008.

[20] X.-z. Cui, X.-l. Yin, H. Chang, Y.-l. Guo, Z.-j. Zheng, Z.-w. Sun, G.-y. Liu, and Y.-j. Wang, "Analysis of an adaptive orbital angular momentum shift keying decoder based on machine learning under oceanic turbulence channels," *Optics Communications*, vol. 429, pp. 138–143, 2018.

[21] R. Lane, A. Glindemann, J. Dainty *et al.*, "Simulation of a kolmogorov phase screen," *Waves in random media*, vol. 2, no. 3, pp. 209–224, 1992.

[22] M. Chen, T. Gao, S. Hu, Q. Zeng, L. Liu, and G. Li, "Simulating non-kolmogorov turbulence phase screens based on equivalent structure constant and its influence on simulations of beam propagation," *Results in physics*, vol. 7, pp. 3596–3602, 2017.

[23] V. I. Tatarski, *Wave propagation in a turbulent medium*. Courier Dover Publications, 2016.

[24] L. C. Andrews and R. L. Phillips, *Laser beam propagation through random media*. SPIE press Bellingham, WA, 2005, vol. 152.

[25] W. Cheng, J. W. Haus, and Q. Zhan, "Propagation of scalar and vector vortex beams through turbulent atmosphere," in *Atmospheric Propagation of Electromagnetic Waves III*, vol. 7200. International Society for Optics and Photonics, 2009, p. 720004.

[26] L. C. Andrews, "An analytical model for the refractive index power spectrum and its application to optical scintillations in the atmosphere," *Journal of Modern Optics*, vol. 39, no. 9, pp. 1849–1853, 1992.

[27] S. Zhao, J. Leach, L. Gong, J. Ding, and B. Zheng, "Aberration corrections for free-space optical communications in atmosphere turbulence using orbital angular momentum states," *Optics express*, vol. 20, no. 1, pp. 452–461, 2012.

[28] J. D. Schmidt, "Numerical simulation of optical wave propagation with examples in matlab." SPIE Bellingham, Washington, USA, 2010.

[29] Z. Yu, T. Qiuyan, W. Jin, and S. Quan, "Numerical simulator of atmospherically distorted phase screen for multibeam time-dependent scenario," *Applied optics*, vol. 53, no. 22, pp. 5008–5015, 2014.

[30] S. Zhao, L. Wang, L. Zou, L. Gong, W. Cheng, B. Zheng, and H. Chen, "Both channel coding and wavefront correction on the turbulence mitigation of optical communications using orbital angular momentum multiplexing," *Optics Communications*, vol. 376, pp. 92–98, 2016.

[31] A. Munkhbayar, O. Nyam-Erdene, H. Kishikawa, N. Goto, and S. Ganbold, "Waveguide-type optical circuits for recognition of optical 8psk-coded labels," *Japanese Journal of Applied Physics*, vol. 58, p. Part 1 (Special Issues), 2019.

[32] H. Hiura and N. Goto, "All-optical label recognition using self-routing architecture of mach-zehnder interferometer optical switches with semiconductor optical amplifiers," *IEICE transactions on electronics*, vol. 90, no. 8, pp. 1619–1626, 2007.

[33] Y. Makimoto, H. Hiura, N. Goto, and S.-I. Yanagiya, "Waveguide-type optical circuit for recognition of optical qpsk coded labels in photonic router," *Journal of Lightwave Technology*, vol. 27, no. 1, pp. 60–67, 2009.

[34] H. Hiura, N. Goto, and S.-i. Yanagiya, "Wavelength-insensitive integrated-optic circuit consisting of asymmetric x-junction couplers for recognition of bpsk labels," *Journal of Lightwave Technology*, vol. 27, no. 24, pp. 5543–5551, 2009.

[35] H. Kishikawa, Y. Makimoto, K. Inoshita, S. Igarashi, N. Goto, and S.-i. Yanagiya, "Improvement of contrast ratio in quadriphase-shift-keying optical label recognition with passive optical waveguide circuit," *Optical Engineering*, vol. 55, no. 5, p. 057104, 2016.

[36] D. Stowe and T.-Y. Hsu, "Demodulation of interferometric sensors using a fiber-optic passive quadrature demodulator," *Journal of Lightwave Technology*, vol. 1, no. 3, pp. 519–523, 1983.

[37] H. Kishikawa, T. Kondo, N. Goto, and S. Talabattula, "Optical thresholder consisting of two cascaded mach–zehnder interferometers with nonlinear microring resonators," *Optical Engineering*, vol. 56, no. 8, p. 086101, 2017.

List of achievements

Publication

1. Munkhbayar Adiya, Nyam-Erdene Odbayar, Hiroki Kishikawa, Nobuo Goto and Ganbold Shagdar, "Waveguide-Type Optical Circuits for Recognition of Optical 8PSK-Coded Labels", Japanese Journal of Applied Physics, Part 1 (Special Issues), Vol.58, No.SJ, SJJA01-1-SJJA01-8, 2019.

2. Munkhbayar Adiya, Hiroki Kishikawa, Nobuo Goto and Ganbold Shagdar, "8-ary OAM shift keying for free-space optical communication system", Optical Engineering, Vol.59,No.2, 026102, 2020.

International conferences

1. Munkhbayar Adiya, Hiroki Kishikawa and Nobuo Goto, "8-ary Orbital Angular Momentum Shift Keying Using 8PSK Recognition Circuit for FSO Communication", OSA Advanced Photonics Congress 2018, No.SpTh3G.4, Zurich, Switzerland, Jul. 2018.

2. Nyam-Erdene Odbayar, Munkhbayar Adiya, Hiroki Kishikawa, and Nobuo Goto, "Proposal of Integrated-Optical Circuit for Recogntion of 8PSK-Coded Label for Photonic Router," 13th Pacific Rim Conference on Lasers and Electro-Optics, Hong Kong, W4J.7, 29 July - 03 August, 2018.

3. Munkhbayar Adiya, Nyam-Erdene Odbayar, Hiroki Kishikawa, and Nobuo Goto, "Optical Waveguide-Type Circuit for Recognition of Two-Symbol 8PSK-Coded Labels from Maximum-Output" 23th MicroOptics Conference (MOC) 2018, Taipei, Taiwan, J-3, 15-18, October, 2018.

4. Munkhbayar Khurelbaatar, Munkhbayar Adiya, Hiroki Kishikawa and Nobuo Goto, "Atmospheric turbulence effects on LG-beam based OAM transmission for OAM shift keying", 5th International Forum on Advanced Technologies (IFAT2019), No.FS32, Taipei, Mar. 2019.

5. Munkhbayar Adiya, Nyam-Erdene Odbayar, Hiroki Kishikawa and Nobuo Goto, "Proposal of Integrated-Optical Circuit for Recognition of 8PSK-Coded", European Conf. on Integrated Optics (ECIO2019), No.W.Po1.29, Ghent, Belgium, Apr. 2019.

6. Munkhbayar Adiya, Hiroki Kishikawa and Nobuo Goto,"8-ary OAM shift keying for FSO link with atmospheric turbulence", OSA 2019 Advanced Photonics Congress (AP2019), San Francisco, No.SpTh3E.6, Jul. 2019.

7. Munkhbayar Adiya, Hiroki Kishikawa and Nobuo Goto, "Efficient decoding method for M-ary OAM shift keying in FSO link", 24th MicroOptics Conference (MOC2019), Toyama, No.P-45, Toyama, Nov. 2019.

8. Munkhbayar Adiya, Hiroki Kishikawa and Nobuo Goto, "Optical signal transmission with 8-ary OAM shift keying through the FSO communication link with phase distortion", 6th International Forum on Advanced Technologies (IFAT2020), Tokushima, Japan, Mar. 2020 (submitted).